NONLOCAL PLASTICITY, INSTABILITY, AND WELL-POSEDNESS OF THE ELASTIC-PLASTIC INITIAL-BOUNDARY VALUE PROBLEM

by

Jeffrey A Burghardt

A dissertation submitted to the faculty of
The University of Utah
in partial fulfillment of the requirements for the degree of

Doctor of Philosophy

Department of Mechanical Engineering

The University of Utah

December 2011

The University of Utah Graduate School

STATEMENT OF DISSERTATION APPROVAL

The dissertation of **Jeffrey A Burghardt**

has been approved by the following supervisory committee members:

Rebecca Brannon	, Chair	**8/12/2011** Date Approved
Daniel Adams	, Member	**8/12/2011** Date Approved
Robert Stoll	, Member	**8/12/2011** Date Approved
James Guilkey	, Member	**8/12/2011** Date Approved
Scott Bardenhagen	, Member	**8/2/2011** Date Approved

and by **Timothy Ameel** , Chair of

the Department of **Mechanical Engineering**

and by Charles A. Wight, Dean of The Graduate School.

ABSTRACT

Traditional associative plasticity theories have previously been shown to be incompatible with experimental data. For this reason, a nonassociative plasticity theory is commonly adopted. Nonassociative plasticity theories are prone to several forms of instability that result in the governing equations becoming ill-posed. Two of these instabilities are discussed: the localization instability and the Sandler-Rubin instability, which is a nonphysical instability that may occur with any degree of nonassociativity.

The primary purpose of this dissertation is to describe how traditional nonassociative plasticity theory can be reformulated to eliminate the Sandler-Rubin instability while maintaining agreement with experimental data. Numerical and analytical techniques are used to investigate the effects of three nontraditional plasticity models on the existence of the Sandler-Rubin instability: viscoplasticity, incrementally nonlinear plasticity, and nonlocal plasticity. Of these, it is shown that only incremental nonlinearity eliminates the instability while maintaining agreement with existing experimental data. Standard laboratory tests cannot detect nonlinearity in a material's incremental response. For this reason a new experimental method and a new data analysis technique are presented and used to validate incrementally nonlinear plasticity theory. The new technique uses a cyclic load path and an interpolation scheme to infer the material response to several loading directions at the same material state. This new technique was used to study the incremental response of aluminum 6061-T0. The new technique suggests that there is significant nonlinearity in the incremental response of this material.

Though it will be demonstrated that the Sandler-Rubin instability is not eliminated with nonlocal theory, this theory is nevertheless well established at regularizing otherwise ill-posed localization problems. Few efficient numerical schemes exist for

solving the equations of nonlocal plasticity. Schemes have previously been developed for solving these equations as part of a finite-element or element-free Galerkin method, but no general convergence criterion had been developed for these methods. A new numerical scheme for solving these equations using the material point method (MPM) is presented. The new scheme uses the MPM background grid for particle-to-particle communication, and results in a simple, matrix-free algorithm. A convergence criterion derived for the new method is furthermore shown to be applicable to some of the methods developed by other researchers.

CONTENTS

Chapters

LIST OF FIGURES

LIST OF SYMBOLS

Symbol	Name and Definition	SI Units	Key Eqn.
$\alpha(\boldsymbol{x})$	Nonlocal weighting function	unitless	4.25
$\boldsymbol{A}$	Acoustic tensor, $\boldsymbol{A} = \boldsymbol{n} \cdot \mathbb{T} \cdot \boldsymbol{n}$	Pa	1.7
β	Friction parameter	unitless	2.3
β_p	Dilatation parameter	unitless	4.35
$\mathbb{C}$	Elastic tangent stiffness tensor	Pa	1.5
De	Deborah number	unitless	2.11
$\dot{\boldsymbol{\epsilon}}$	Total strain rate tensor	1/s	1.1
$\dot{\boldsymbol{\epsilon}}^e$	Elastic strain rate tensor	1/s	1.1
$\dot{\boldsymbol{\epsilon}}^{\mathrm{vp}}$	Viscoplastic strain rate tensor	1/s	2.10
$\dot{\boldsymbol{\epsilon}}^p$	Plastic strain rate tensor	1/s	1.1, 1.4
$\dot{\boldsymbol{e}}^*$	Deviatoric part of the strain rate tensor	1/s	2.7
$\dot{e}_v$	Volumetric strain rate	1/s	2.7
f	Yield function	Pa	1.2
$\boldsymbol{f}_i^{\mathrm{int}}$	Nodal internal force vector	N	4.3
g	Plastic flow potential function	Pa	1.6
h	Hardening modulus	Pa	2.13,2.14
I_1	First stress invariant, $I_1 = \mathrm{Tr}(\boldsymbol{\sigma})$	Pa	2.3
$\boldsymbol{I}$	Second-order identity tensor	unitless	2.7
J_2	Second invariant of the deviatoric stress tensor, $J_2 = \frac{1}{2}\boldsymbol{S}{:}\boldsymbol{S}$	Pa^2	2.3
k_{limit}	maximum value of the yield strength	Pa	2.6
k_o	Initial yield strength	Pa	2.3
$\dot{\lambda}$	Magnitude of the plastic strain rate tensor	1/s	1.4
$\langle\dot{\lambda}\rangle$	Nonlocal plastic multiplier	1/s	4.25
$\mathscr{L}$	Lipschitz constant for fixed-point system	unitless	4.42
L	Nonlocal length scale	m	2.15
$\hat{\boldsymbol{M}}$	Direction of plastic strain rate	unitless	1.6
m	Overlocal parameter	unitless	2.12
m_i	Nodal mass	kg	4.4
$\hat{\boldsymbol{N}}$	Unit normal to the yield surface	Pa	1.4
N_α	Number of particles within the support of $\alpha(\boldsymbol{x})$	unitless	4.42
P_t^v	Volumetric incremental nonlinearity parameter	unitless	2.7
P_t^*	Deviatoric incremental nonlinearity parameter	unitless	2.7

ϕ_{ip}	MPM mapping function between the ith node and the pth particle	unitless	4.6
ρ	Mass density	kg/m^2	4.1
$\dot{\boldsymbol{\sigma}}$	Stress rate tensor	Pa	1.5
$\boldsymbol{\sigma}$	Stress tensor	Pa	1.5
σ_z	Axial Lode invariant	Pa	3.10
σ_r	Radial Lode invariant	Pa	3.10
$\boldsymbol{S}$	Deviatoric stress tensor, $\boldsymbol{S} = \boldsymbol{\sigma} - \frac{1}{3}\text{Tr}(\boldsymbol{\sigma})\boldsymbol{I}$	Pa	-
S_ϵ	Directional stiffness	Pa	2.4
S_ϵ^e	Elastic directional stiffness	Pa	2.5
$\dot{\boldsymbol{\sigma}}_\epsilon$	Projection of stress onto strain rate direction	Pa	2.4
$\boldsymbol{\sigma}^{\text{over}}$	Overstress tensor, $\boldsymbol{\sigma}^{\text{over}} = \boldsymbol{\sigma} - \boldsymbol{\sigma}^{\text{qs}}$	Pa	2.8
$\boldsymbol{\sigma}^{\text{qs}}$	Quasistatic stress tensor	Pa	2.8
τ_{mat}	Plastic relaxation time	s	2.10
τ_{load}	Characteristic loading time	s	2.11
$\mathbb{T}$	Plastic tangent stiffness tensor	Pa	2.5,3.14
z	Cumulative equivalent plastic strain	unitless	2.6
z_{ref}	Nonlinear hardening parameter	unitless	2.6
ζ	Nonlocal hardening/softening internal state variable	Pa	2.12

ACKNOWLEDGEMENTS

CHAPTER 1

INTRODUCTION AND LITERATURE
REVIEW

1.1 Introduction

Numerical simulations can play an important role in the analysis and design of safe and efficient mechanical systems and structures. A crucial part of any numerical simulation is the constitutive model, which describes the material's mechanical response to the loading. Together with the equations of motion, and appropriate boundary and initial conditions, the constitutive model completes a solvable set of equations. To be most useful in predicting the behavior of a system, the equations must be well-posed. Here, well-posedness is to be understood as defined by Hadamard [1], who argued that the set of equations used to model a physical system ought to have a unique solution for which small changes in the problem data produce small changes in the solution. Equations that do not have these properties are called ill-posed. Such equations are of limited use in engineering analysis since any solution that is found cannot be reliably used to predict the behavior of a system because the solution is either not unique, or is chaotic because of sensitivity to small changes in the problem data. In some cases chaotic behavior is observed in the laboratory, while other instances of ill-posed governing equations are the result of an incomplete model or the use of inappropriate assumptions. In cases where the ill-posedness is descriptive of an actual phenomenon, nonunique or chaotic solutions may still provide useful information, but interpreting the solutions often becomes much less straightforward than with a unique solution. A classic example of a problem with extreme sensitivity to problem data is a buckling problem. At the onset of buckling, the problem becomes ill-posed because minute defects in the material can drastically affect the solution. Therefore, it is very difficult

to predict the behavior of a structure after the onset of buckling. Therefore, a model of a buckling structure is of limited usefulness to predict a structure's response after the onset of buckling with any degree of certainty, although the model may be used to accurately predict the onset of buckling. This dissertation describes several classes of engineering problems that are ill-posed when a classical plasticity constitutive model is used in the analysis.

Plasticity models are commonly used to model a broad range of engineering materials, including metals, ceramics, concrete, and rocks. Sections 1.2 and 1.3 provide an overview of classical plasticity theory, and Section 1.4 introduces several ways that classical plasticity theory may result in an ill-posed set of governing equations. The plastic instability of primary interest in this dissertation is the Sandler-Rubin instability. As described in Chapter 2, this instability is not observed in the laboratory. The primary purpose of this dissertation is to examine several ways of reformulating classical plasticity theory, and to determine which, if any, of these reformulations eliminate the Sandler-Rubin instability and restores the well-posedness to problems where this instability is manifest.

A secondary purpose of this dissertation is to present a new numerical technique for solving the equations of nonlocal plasticity. Nonlocal plasticity theory has become well established as a means of restoring the well-posedness to otherwise ill-posed localization problems. As will be discussed in Chapter 4, the instability resulting from localization is observed in laboratory tests, but when a classical plasticity theory is used, localization problems are mathematically ill-posed, and possess solutions that are not descriptive of behavior observed in laboratory tests. Nonlocal theory restores the well-posedness to these problems by including additional physics (microstructural effects) that are not present in classical plasticity theory.

Restoring the well-posedness to these problems would allow the development of predictive simulations for problems where it is currently not possible. The primary types of problems that may benefit from the new contributions in this dissertation are problems involving wave propagation or localization of frictional materials such as geologic materials.

1.2　Classical Plasticity Theory

Classical plasticity theory assumes that the strain rate tensor $\dot{\boldsymbol{\epsilon}}$ may be decomposed additively into elastic $\dot{\boldsymbol{\epsilon}}^e$ and plastic $\dot{\boldsymbol{\epsilon}}^p$ parts

$$\dot{\boldsymbol{\epsilon}} = \dot{\boldsymbol{\epsilon}}^e + \dot{\boldsymbol{\epsilon}}^p \tag{1.1}$$

For rate-independent theories, these rates may be regarded as increments with respect to any monotonically increasing parameter.

Classical plasticity theory also relies on the assumption that there exists a set of stress states for which the material behavior is purely elastic. An elastic deformation is defined to be a deformation that is fully reversed when the applied load is released. The set of stress states that may be attained through purely elastic deformation is defined using a scalar yield function f whose arguments are the stress tensor $\boldsymbol{\sigma}$ as well as a set of internal state variables, collectively denoted η, that account for previous loading history. The yield function is defined such that

$$f\dot{\lambda} = 0, \ f \leq 0, \ \dot{\lambda} \geq 0 \tag{1.2}$$

where $\dot{\lambda}$ is the magnitude of the plastic strain rate tensor (i.e., $\dot{\lambda} = \|\dot{\boldsymbol{\epsilon}}^p\|$, where $\|()\|$ indicates the Euclidean norm), and is also sometimes called the plastic multiplier. These conditions are known as the Kuhn-Tucker conditions. According to these conditions, rate-independent plastic flow ($\dot{\lambda} > 0$) may only occur when $f = 0$. The set of all stress states for which $f = 0$ for a given set of internal state variable values, forms an isosurface in six-dimensional stress space, which is called the yield surface. For isotropic models, the yield surface may be visualized as a surface in three-dimensional principal stress space. The Kuhn-Tucker conditions require that the stress state remain on the yield surface while the material is undergoing plastic deformation, although the yield surface may expand, contract, or change shape while undergoing plastic deformation. Finally, the Kuhn-Tucker conditions require that the yield function have a negative value when the stress state lies within the yield surface.

In plasticity theory, the flow rule is an equation that defines the "direction" of the plastic strain rate tensor. The direction of a tensor $\boldsymbol{T}$ is defined by the unit tensor $\hat{\boldsymbol{T}}$ given by

$$\hat{T} = \frac{T}{\|T\|} \tag{1.3}$$

Classical plasticity theory assumes the existence of a "regular" flow rule, which means that the direction of the plastic strain rate tensor is not a function of the total strain rate tensor itself. Traditionally, the plastic strain rate direction is chosen to be in the direction of the yield surface normal $N = \frac{\partial f}{\partial \sigma}$, so that the flow rule becomes

$$\dot{\epsilon}^p = \dot{\lambda} \hat{N} \tag{1.4}$$

where here, and in what follows, a circumflex indicates normalization so that, in this case, $\hat{N}$ is defined to be N divided by its own magnitude. This type of flow rule is called an associative flow rule, since the plastic flow direction is associated with the yield surface normal.

The final governing equation of classical plasticity theory is the elasticity equation, in which the stress rate $\dot{\sigma}$ arises from the elastic part of the strain rate tensor according to

$$\dot{\sigma} = \mathbb{C} \colon \dot{\epsilon}^e \tag{1.5}$$

where $\mathbb{C}$ is the fourth-order elastic tangent stiffness tensor. Note that the elasticity equation represents a linear relationship between the stress rate and the strain rate, which exists even for nonlinear elasticity. Extensions to classical plasticity theory occasionally include additional terms in Eq. (1.5) that accommodate additional dependence of the stress rate on the internal state variables (allowing, for example, elastic stiffening with pore collapse and allowing elastic softening with dissipative heating). As discussed by Brannon [2], such terms lead to an apparent nonassociativity of the stress increment even if the flow rule is associative.

1.3 Nonassociative Flow Rules

The classical plasticity theory just described was originally developed to describe the behavior of metals subjected to relatively small changes in pressure, where the von Mises or Tresca yield criterion is often used. As interest grew in applying plasticity theory to a broader class of materials and loading conditions, Drucker and Prager [3] extended the von Mises yield criterion to allow a pressure dependent yield strength.

An important consequence of using an associative flow rule in material models with a pressure dependent yield strength is that plastic dilatation (volume increase) results from shear loading. While plastic dilatation is often observed in many materials, the plastic dilatation predicted by an associative flow rule has been shown to be 10-20% greater than what is actually observed in laboratory tests of geologic materials [4, 5]. For metals at low pressure, the yield strength has been shown to be pressure dependent while little or no plastic dilatation is observed [6, 7, 8, 9]. Since with an associative flow rule, the degree of plastic dilatation is proportional to the pressure dependence of the yield strength, nearly zero dilatation and a pressure-dependent yield strength are incompatible with an associative flow rule.

Because associative flow rules generally overpredict the amount of plastic dilatation, a nonassociative flow rule is often adopted. A nonassociative flow rule takes the direction of the plastic strain rate to be normal to the isosurfaces of a function of the stress tensor called the plastic flow potential function g. The unit normal to the isosurfaces of g is $\hat{\boldsymbol{M}}$. Therefore, the nonassociative flow rule is

$$\dot{\boldsymbol{\epsilon}}^p = \dot{\lambda}\hat{\boldsymbol{M}} \tag{1.6}$$

Note that a nonassociative flow rule is still classified as a regular flow rule, since the direction of plastic flow $\hat{\boldsymbol{M}}$, is still independent of the direction of $\dot{\boldsymbol{\epsilon}}$.

A nonassociative flow rule allows the yield function parameters to be chosen independently of the plastic flow potential function parameters. Therefore, a nonassociative flow rule allows the yield function to be pressure dependent, while the plastic flow potential function can be chosen to have a lesser degree of pressure dependence, and thereby reduce the amount of plastic dilatation predicted by the model. Because of this, nonassociative flow rules have been shown to fit experimental data better than associative flow rules [6, 4, 10, 11]. However, the data supporting nonassociative flow rules are invariably measured under conditions of constant loading trajectory in stress space. Such testing provides no validation of the regular flow rule itself, which (as discussed in Chapter 2) must be assessed by measuring material response to changes in the loading direction.

1.4 Consequences of Nonassociative Plasticity: Ill-Posedness and Instability

While a nonassociative flow rule has been shown to be capable of fitting experimental data more accurately than an associative model, nonassociative flow rules have also been shown to give rise to several forms of instability and ill-posedness. Associative plasticity theories have been shown to result in stable, unique solutions to the equations of motion or equilibrium so long as the hardening modulus h is positive or zero [12]. As discussed in detail in [2], the consistency condition that requires stress to remain on the yield surface leads to the requirement that $\dot{\boldsymbol{\sigma}}{:}\hat{\boldsymbol{N}} = h\dot{\lambda}$, where h is the hardening modulus (determined from the combined effect of changes of internal variables in response to plastic loading). Therefore, since plastic loading always involves $\dot{\lambda}$, this implies that the normal component of the stress rate (i.e., the yield surface motion) is outward (hardening) if $h > 0$ and inward (softening) if $h < 0$. A subtle point regarding the stability of plastic boundary-value problems with a positive hardening modulus is that a structural problem involving a "stable" material model may nonetheless become unstable and ill-posed (such as the buckling example mentioned in Section 1.1). Therefore, what is meant here is that with an associative flow rule with a positive hardening modulus, the constitutive model is not inherently unstable.

When softening occurs, the tangent modulus for some loading directions can become negative, which results in a imaginary wave speed and a loss of hyperbolicity for the equations of motion, or a loss of ellipticity for the equations of equilibrium [12, 13, 14]. The plastic wave speeds in a given direction $\boldsymbol{n}$ (a unit vector), correspond to the eigenvalues of the acoustic tensor $\boldsymbol{A}$ associated with the fourth-order plastic tangent stiffness tensor $\mathbb{T}$. The acoustic tensor is defined as

$$\boldsymbol{A} = \boldsymbol{n} \cdot \mathbb{T} \cdot \boldsymbol{n} \tag{1.7}$$

For an associative plasticity model without elastic-plastic coupling [15], the acoustic tensor is symmetric, and with $h \geq 0$, it is also positive definite. For $h < 0$, the acoustic tensor is no longer positive definite. When this occurs, the governing equations

become ill-posed, which is generally manifest in numerical solutions by a lack of convergence [14, 16].

Drucker [13] proposed a criterion for the loss of stability caused by a constitutive model. This is called Drucker's stability postulate, and requires that

$$\dot{\boldsymbol{\sigma}}{:}\dot{\boldsymbol{\epsilon}}^p \geq 0 \tag{1.8}$$

for stability. Drucker's stability postulate is essentially equivalent to Hill's [12] second-order work-rate criterion[1]

$$\dot{\boldsymbol{\sigma}}{:}\dot{\boldsymbol{\epsilon}} \geq 0 \tag{1.9}$$

which Hill proved to be a sufficient condition for the existence and uniqueness of elastic-plastic boundary value problems. This is not a necessary condition for uniqueness, since Hill and Drucker's criteria may be violated before a loss of hyperbolicity occurs [14].

Il'iushin [17] proposed a stability postulate that is less restrictive than Drucker's postulate. Il'iushin's stability postulate states that for a stable material, there cannot exist closed strain paths from which positive net work can be extracted from the material. As will be discussed in Section 1.4.2, such strain paths exist for nonassociative plasticity models.

Replacing an associative flow rule with an nonassociative flow rule radically changes the character of the governing equations. For example, with a nonassociative flow rule, both $\mathbb{T}$ and $\boldsymbol{A}$ are not symmetric as they are with an associative flow rule without elastic-plastic coupling [15]. With the loss of symmetry, the acoustic tensor may no longer be positive definite, even with a positive value of the hardening modulus. Neilsen and Schreyer [18] have shown that loss of hyperbolicity occurs with a nonassociative model when the smallest eigenvalue of the symmetric part of the acoustic tensor becomes negative or zero. As a result of this change in the governing equations, several forms of instability and nonuniqueness have been shown

---

[1]Note that what is called the second-order work rate does not have the units of work/time, and is therefore not actually a work rate. It is, however, the coefficient of the second-order term in the Taylor series of the work rate.

to be possible with nonassociative plasticity models. Each subsection below describes one of these possible instabilities.

1.4.1 Localization Instability

As mentioned in Section 1.4, when $h < 0$ the equations of motion lose hyperbolicity. Hill [12] connected this change in the governing equations with the onset of localization. Localization refers to increases in the strain field that occur only within a discrete region of a structure as the loading continues. A familiar example of localization is the necking of a steel bar in a uniaxial stress tension test. Rudnicki and Rice [19] have shown that with a nonassociative flow rule, localization, and the resulting instability and ill-posedness, may occur even while the material remains in the hardening regime. This means that for certain loading directions, a nonassociative model will predict a softening-like behavior, even with a positive value of the hardening modulus [20]. It has been shown that there exists a critical value for the hardening modulus, above which localization is precluded [20, 21]. A related instability exhibited by nonassociated models occurs when two of the eigenvalues of the acoustic tensor become a complex-conjugate pair [22, 23]. This may occur prior to the onset of localization. Experimental data suggest the onset of localization within the hardening regime is a real phenomenon [24, 25, 26, 27], and that a realistic constitutive model for materials that exhibit shear banding (such as geologic materials) should admit this instability.

In a real material, the microstructural "texture" of the material plays an important role in determining the size and nature of the localization region [28]. Localization problems are ill-posed because traditional local constitutive models possess no intrinsic length scale, and hence no microstructural effects. Consequently, the localization zone collapses unrealistically to a zone of zero volume [29]. Furthermore, zero energy is dissipated in the infinitesimally small localization region. In simulations, this localization zone collapses to the smallest element size [30], and the failure energy approaches zero as the mesh is refined. However, in laboratory observations the localization zone has a finite and reproducible width.

Even though the localization instability is a real phenomenon, the governing

equations must, nevertheless, be reformulated in some manner to create a well-posed set of governing equations. One common regularization method is to use a nonlocal plasticity model, possibly in combination with a realistic spatial perturbation to induce a unique realization belonging to an infinite set of possible solutions (similar to perturbing a column to induce buckling in one out of an infinite number of possible directions). Chapter 4 contains a description of this theory, and also presents a new method for solving the resulting constitutive equations using the material point method.

1.4.2 Sandler-Rubin Instability

While the localization instability can occur in nonassociative models because of the softening-like behavior that they predict for certain loading directions, nonassociative models also predict a stiffening behavior for other loading directions [20]. Specifically, for certain loading directions, the plastic tangent modulus exceeds the elastic tangent modulus. It has been shown that this stiffening behavior is possible with any nonassociative model [15]. The result is that there are closed strain paths for which positive net work can be extracted from a material. This is a violation of both Drucker's stability postulate, and the more restrictive Il'iushin stability postulate [17]. While the knowledge that such load paths existed led to some concern about a possible loss of stability, no specific mathematical example of this theoretical instability was found until the 1987 paper by Sandler and Rubin. While this example demonstrates that the instability of nonassociative plasticity exists in theory, subsequent discussions below argue that, unlike the localization instability (which has been observed), the Sandler-Rubin instability is not expected to exist in reality. Accordingly, revisions of classical plasticity will be sought to eliminate the Sandler-Rubin instability.

Lade conducted triaxial compression tests in which sand specimens were shown to exhibit apparent nonassociative behavior [4]. Samples of the same material were then loaded in directions for which a violation of Drucker's postulate would be expected. No obvious unusual collapse of the specimens was observed, which was taken as evidence that Drucker's postulate may be violated without inducing any instability. The study did not, however, actually measure plastic strain increments to verify that

Drucker's postulate was violated, but instead fit a nonassociative plasticity model to the triaxial compression data. The direction of the plastic strain increment was then inferred from the standard triaxial compression tests. This procedure itself assumes the existence of a regular flow rule. Furthermore, as was shown by Sandler and Rubin [31], the instability resulting from this stiffening behavior does not produce a "gross collapse" as was anticipated by Lade. Instead this instability, if it exists in real materials, would be observed in the unstable growth of propagating waves.

Until the work of Sandler, Rubin and Pučik [31, 32], all arguments as to the existence of an instability related to this stiffening behavior had been based upon abstract theoretical arguments. Sandler and Rubin devised a case study problem for which an analytic solution exists that clearly illustrated the existence of the instability and some of its salient features. Sandler and Rubin showed that their case study problem is ill-posed and possesses an infinite number of solutions. In a paper that is currently under review, Pučik, Brannon and Burghardt showed how this instability and nonuniqueness can be observed in finite-element simulations [16]. Specifically, it was found that both the amplitude and width of a propagating wave may increase in finite-element solutions with a nonassociative model, and that the nonuniqueness is manifest primarily through a mesh dependency of the solution. In a companion paper that is also currently under review, and appears as Chapter 2 of this dissertation, Burghardt and Brannon use this same case study to investigate several nontraditional plasticity models to determine if they also admit this instability. These nontraditional plasticity models include an incrementally nonlinear model, a viscoplastic model, and a nonlocal model, each of which is described in detail in Chapter 2. In that chapter the author demonstrates that, of the models considered, only the incrementally nonlinear model is capable of eliminating the instability while maintaining agreement with laboratory data. Chapter 3 describes the results of a validation study of incrementally nonlinear models for aluminum 6061-T0. The validation study suggests that an incrementally nonlinear model is applicable to this material. As part of the study presented in Chapter 2, a new method was developed for solving the equations of nonlocal plasticity with the material point method (MPM). A description of this new numerical technique is presented in Chapter 4.

CHAPTER 2

NONUNIQUENESS AND INSTABILITY OF CLASSICAL FORMULATIONS OF NONASSOCIATIVE PLASTICITY: EFFECT OF NONTRADITIONAL PLASTICITY FEATURES ON THE SANDLER-RUBIN INSTABILITY

2.1 Abstract

The Sandler-Rubin instability is a dynamic instability resulting from nonassociative plastic flow. This instability allows stress waves to grow in both amplitude and width as they propagate. In addition to this physically implausible behavior, multiple solutions to the equations of motion have been shown to exist when the instability occurs. Reformulation of some aspects of traditional plasticity theory is necessary since associative models overpredict the amount of plastic dilatation, and nonassociative models may result in this physically unrealistic behavior. The purpose of this paper is to investigate the effects of various traditional and nontraditional plasticity features on the existence of the instability and resulting nonuniqueness. Using a simple case study, the instability and nonuniqueness are shown to persist with both linear and nonlinear hardening and softening. An incrementally nonlinear model is shown to eliminate the instability and result in mesh-independent solutions. A viscoplastic model is shown to lead to unstable solutions for all loading rates. However, mesh-independent unstable numerical solutions are found when the loading time scale is much less than the plastic relaxation time. A nonlocal plasticity model is

shown to produce solutions that are both unstable and mesh dependent. Therefore, of the models considered, only the incrementally nonlinear model was capable of eliminating this nonphysical instability. This work provides much needed direction for laboratory investigations of the validity of incrementally nonlinear flow rules.

2.2   Introduction

An associative plasticity model is one for which the plastic strain rate tensor is proportional to the normal to the yield surface. While associativity has been shown to be a sufficient condition for the existence and uniqueness of solution for boundary value problems [12], several studies have demonstrated that associative flow rules are incompatible with experimental data. Specifically, Spitzig and Richmond [7] showed that associative models overpredict the amount of plastic dilatation in triaxial compression tests of metals. Lade [4] found a similar problem with associative flow rules for geologic materials. More recently, Stoughton [33] and Mohr [11] have shown that associative flow rules do not accurately describe the anisotropic plastic flow of sheet metals.

For these reasons, nonassociative models have become increasingly popular. A nonassociative model allows the yield strength and plastic flow direction to be independently prescribed. This allows the dilatation and frictional angles to be independently prescribed and thereby tuned to correctly fit the plastic dilatation observed in triaxial compression tests. For anisotropic sheet metals a nonassociative flow rule allows the degree of anisotropy of the yield function and the plastic flow potential function to be independently tuned to match experimental data. This capability has been demonstrated to lead to a significant improvement in the ability of plasticity models to fit experimental data [11, 10, 34].

These studies have consistently demonstrated that an associative flow rule is incompatible with experimental data, and that a nonassociative flow rule results in a model with more mathematical flexibility, and therefore can be more accurately tuned to experimental data. Despite this fact, the adoption of a nonassociative model brings with it a host of possible problems. For example, nonassociative models do not satisfy Drucker's stability postulate for all loading directions [13]. Of course,

Drucker's stability postulate has been proven to be only sufficient, but not necessary, for stability and uniqueness [12]. As discussed in detail below, nonassociative models have been shown to result in instability and a loss of uniqueness for certain loading conditions.

A well-known loading condition that results in loss of uniqueness and instability with a nonassociative flow rule was discovered by Rudnicki and Rice [19]. They showed that under certain loading directions, a nonassociative model could result in a localization instability even while the material remained in the hardening regime. This localization instability has been shown to result in a loss of uniqueness of solution for local rate-independent plasticity models. This instability and nonuniqueness have been extensively studied over the years [28, 30, 35, 36]. Experimental data suggest that real materials exhibit hardening behavior for some loading direction, and localize for other loading directions [24, 25, 26], which is consistent with the existence of the softening-like behavior of nonassociative models. While the softening-like behavior of nonassociative models is consistent with experimental data, the governing equations are nevertheless ill-posed with the onset of localization and must be reformulated in some way to produce a well-posed problem. The current leading approaches are nonlocal plasticity and gradient plasticity.

Another, and fundamentally different, source of instability and nonuniqueness caused by nonassociative plastic flow was first observed by Sandler and Rubin [31]. They showed that with any degree of nonassociativity there exist loading directions for which the wave speed in plastic loading exceeds the wave speed in elastic unloading. This over-stiffening occurs any time the trial stress rate tensor has a positive inner product with the normal to the yield surface, but a negative inner product with the plastic strain rate tensor. This region of stress space, which lies above the yield surface, but below the plastic flow potential surface, will be herein referred to as the Sandler-Rubin wedge. Sandler and Rubin showed that the existence of these so-called "fast plastic" waves causes a loss of uniqueness of solutions and that solutions are admitted for which an infinitesimal stress perturbation can nonphysically grow in amplitude and width as it propagates. This phenomenon is essentially equivalent to spontaneous motion from a quiescent state, which can be construed as an implausible

behavior for a passive material.

The numerical manifestation of the ill-posedness caused by the Sandler-Rubin instability is remarkably similar to that caused by localization. Specifically, when a local model is used to solve a localization problem, the strain in the localization region becomes unbounded with mesh refinement. For localization problems, the region of unbounded strain is stationary in a Lagrangian sense. For the Sandler-Rubin instability, the region of unbounded strain lies at the peak of a propagating stress wave. As the head and tail of the wave diverge because of the inversion in elastic and plastic wave speeds, the region of unbounded strain expands linearly in time. In the one-dimensional case study considered here, the solution in this region of space has been previously shown [16] to be subject to only two constraints:

$$0 \leq \dot{\boldsymbol{\sigma}} \tag{2.1}$$

and

$$C_E < v < C_P \tag{2.2}$$

where $\dot{\boldsymbol{\sigma}}$ is the axial component of the stress rate, C_E is the elastic wave speed, v is the wave speed in the region of nonuniqueness, and C_P is the plastic wave speed.

In a relatively recent series of articles on plastic stability, Stoughton and coauthors [37, 38] have expressed some concerns about the range of validity of Sandler and Rubin's analysis. Most recently, Stoughton [38] has suggested that the Sandler-Rubin instability is permitted by only a very small and simple subset of nonassociative plasticity models. In this paper it is shown why this concern is not warranted, and that the instability and nonuniqueness persist for nearly all nonassociative plasticity models.

In light of both the loss of uniqueness of solution and the physically implausible behavior permitted under the Sandler-Rubin instability, it seems that traditional nonassociative models must be rejected. However, as discussed previously, associative models also must be rejected since they are incompatible with experimental data. Clearly a resolution to this problem lies outside of traditional plasticity theories. The purpose of this paper is to investigate several nontraditional theories to determine

which, if any, of these theories are capable of matching experimental data while at the same time eliminating the physically implausible Sandler-Rubin instability.

In a previous paper by Pučik, Brannon and Burghardt [16], the existence and characteristics of the Sandler-Rubin instability were illustrated using both analytical and numerical solutions to a simple one-dimensional wave-propagation problem. To illustrate the instability in the simplest possible context, the previous paper employed a rate-independent, perfectly-plastic model. In this paper we solve this same case study with a variety of generalizations of this simple model.

The case study is briefly described in Section 2.3. In Section 2.5, we examine various generalizations of the simple plasticity model considered in [16]. The first of these generalizations discussed here is linear and nonlinear hardening and softening. The second reformulation considered is the adoption of an incrementally nonlinear flow rule, which allows the plastic flow direction to change based on the incremental loading direction. The third alternative theory considered is the adoption of rate dependence. The final reformulation of traditional plasticity theory considered here is an integral-type nonlocal plasticity theory.

2.3   Description of the Case-Study Problem

In this section, a simple numerical case study problem is described that elicits the Sandler-Rubin instability. The case study problem consists of a semi-infinite elastic/plastic half space as shown in Fig. 2.1. The axial component of the initial stress state $\boldsymbol{\sigma}_X^*$ is chosen to be $-100\,\text{MPa}$, while the lateral component, $\boldsymbol{\sigma}_Y^* = \boldsymbol{\sigma}_Z^*$, is chosen to be $-17.55\,\text{MPa}$, where stresses are taken to be positive in tension. The material is also assumed to be in a quiescent initial state. The linear Drucker-Prager yield function used in this case study is:

$$f = \sqrt{J_2} + \beta I_1 - k_o \tag{2.3}$$

where $J_2 = \frac{1}{2}\boldsymbol{S}{:}\boldsymbol{S}$, $\boldsymbol{S}$ is the deviatoric stress tensor, $I_1 = \text{Tr}(\boldsymbol{\sigma})$, and β and k_o are material parameters whose values are chosen to be 0.315 and 5.066 MPa, respectively. With these parameters, and the chosen initial stress state, the material is at incipient yield in its initial condition. The dilatation angle is chosen to be zero, meaning that

the plastic strain rate tensor is proportional to the deviatoric part of the stress tensor and therefore has no volumetric part. Various generalizations of this simple model will be considered and are discussed in detail below. This model was contrived to simplistically demonstrate the existence and character of the instability. In what follows, various enhancements to this model are systematically explored to determine their effect on the instability in this case study.

The surface traction at the free surface is initially -100 MPa, which places the material in equilibrium in the initial state. A small perturbation is applied to the surface traction as shown in Fig. 2.1. The perturbation is characterized by the peak change in stress $\sigma_o = 10$ MPa, and the duration of the pulse $\tau = 2$ ms. Since the axial component of stress changes from -100 MPa to -90 MPa, this is a tensile stress increment that reduces both the confining pressure and the magnitude of the stress deviator and induces plastic flow. This loading increment is reversed by returning the axial component of the stress tensor to its initial value in what can be shown to be an elastic recompression increment. This loading sequence results in the triangular-shaped time history of the perturbation shown in Fig. 2.1, with the front of the triangular pulse causing the material to undergo plastic loading and the tail of the pulse causing elastic unloading. Here loading refers to an increment that induces plastic flow and unloading refers to an increment that is purely elastic, even though the plastic loading increment represents a decrease in the applied load.

This perturbation causes a longitudinal wave to propagate through the half space. As shown by Pučik et al. [16] and illustrated in Fig. 2.2, this loading condition places the trial stress rate in the Sandler-Rubin wedge and results in a plastic wave speed that exceeds the elastic wave speed. This case study was also shown to possess a two-parameter family of nonunique analytical solutions. The problem was also solved numerically using the finite-element method. In subsequent work, and as shown in Fig. 2.3, the finite-element results were reproduced using a material point method (MPM) code [39, 40, 41], which is also used in the simulations presented in this paper.

As these solutions illustrate, the head of the wave (left-hand portion of the stress wave history) and the tail of the wave (right-hand portion of the stress wave history) are diverging from each other due to the plastic wave speed exceeding the elastic wave

speed. This causes what is initially a single point at the top of the triangular stress pulse to open up into a finite region. It is in this region that the solution is nonunique. This nonuniqueness becomes apparent in analytical solutions by the presence of free parameters in the solution. In contrast, nonuniqueness can be much more subtle in numerical solutions. As with the nonuniqueness that occurs in localization problems, the numerical manifestation of the Sandler-Rubin instability occurs primarily though a mesh dependency of the solution. This can be observed by comparing the coarse resolution plot on the left-hand side of Fig. 2.3 with the finer resolution on the right-hand side of the same figure. At late times in the more resolved solution, secondary peaks in the stress wave begin to form, which grow much more rapidly than the primary peak. As the mesh is further refined, these secondary peaks begin to form at earlier and earlier times and also grow at an increasingly rapid rate, with the result being that the numerical solution diverges with mesh refinement. The same trend was observed by Pučik et al. [16] using the finite-element method, though the formation of the secondary peaks began at a different mesh resolution.

2.4   Directional Stiffness

The concept of directional stiffness as developed by Runesson [20] is a convenient method for studying the stiffness properties of a plasticity model. The directional stiffness S_ϵ is defined such that

$$\dot{\boldsymbol{\sigma}}_\epsilon = S_\epsilon \dot{\boldsymbol{\epsilon}} \tag{2.4}$$

where $\dot{\boldsymbol{\sigma}}_\epsilon$ is the projection of the stress rate, $\dot{\boldsymbol{\sigma}}$, onto the direction of $\dot{\boldsymbol{\epsilon}}$. The directional stiffness ratio is defined as the ratio of the plastic and elastic directional stiffness:

$$R_\epsilon = \frac{S_\epsilon}{S_\epsilon^e} = \frac{\dot{\boldsymbol{\epsilon}}:\mathbb{T}:\dot{\boldsymbol{\epsilon}}}{\dot{\boldsymbol{\epsilon}}:\mathbb{C}:\dot{\boldsymbol{\epsilon}}} \tag{2.5}$$

where S_ϵ^e is the elastic directional stiffness, $\mathbb{T}$ is the fourth-order elastic-plastic tangent stiffness tensor, and $\mathbb{C}$ is the fourth-order elastic tangent stiffness tensor. This quantity provides a scalar measure of the stiffness of a plasticity model relative to the corresponding elastic stiffness for a given loading direction . As shown in Fig. 2.4, the loading direction is quantified by the loading angle, θ, which is defined such that it is zero when the strain rate tensor is tangent to the yield surface. Of the two tangent

directions, θ is measured from the directional tangent tensor having a negative trace (compressive).

The right-hand side of Fig. 2.4 is a plot of the directional stiffness ratio for both associative and nonassociative, perfectly plastic, linear Drucker-Prager models for $0 \geq \theta \geq \pi/2$. As shown in the figure, the directional stiffness ratio for an associative model is always greater than zero and less than one. However, with a nonassociative model, the directional stiffness ratio is negative for some loading directions, and greater than one for others. This results in the nonassociative model exhibiting a softening-like behavior for certain loading directions, and an over-stiffening behavior for others. The softening-like behavior occurs when the plastic directional stiffness ratio is less than zero, and corresponds to the onset of localization even while the material remains in the hardening regime [19].

In contrast to the softening-like behavior, the over-stiffening behavior of nonassociative models has seen much less study, and its effects are much more subtle. As discussed in Section 2.3, when the over-stiffening behavior occurs, the plastic wave speed exceeds the elastic wave speed, resulting in a loss of uniqueness of solution and the existence of a physically implausible instability. The loss of uniqueness of solution itself is problematic from a practical standpoint as it can result in mesh-dependent numerical solutions, or solutions that are very sensitive to small changes in the input parameters, as is the case with localization problems. However, in contrast to the instability seen in localization problems, the Sandler-Rubin instability is not physically plausible. Therefore, resolving the mesh dependency arising from the Sandler-Rubin instability is not a matter of only restoring the well-posedness, but rather the plasticity model must be modified to preclude the existence of the instability.

Therefore, we draw a conclusion that a realistic plasticity model will have a directional stiffness ratio that is less than zero for some loading directions (and therefore admits localization in the hardening regime), but is never greater than one (and therefore does not admit the Sandler-Rubin instability). We now examine various modifications to the elastic perfectly-plastic model considered thus far to determine which, if either, of these requisite properties each model exhibits.

2.5   Use of Alternative Theories

In what follows, the case study problem is solved using the MPM with various modifications to the nonhardening plasticity model considered by Pučik et al. [16]. Both isotropic hardening and softening are considered, as well as three nontraditional plasticity model formulations. Each subsection describes the model reformulation as well as its effect upon the existence and characteristics of the Sandler-Rubin instability.

2.5.1   Hardening and Softening

In this section we examine the effect of hardening and softening upon the Sandler-Rubin instability. Figure 2.5 shows the directional stiffness ratio for the modified constitutive model, including both hardening and softening. As has been pointed out by Runesson [20] and as witnessed by the increase in the minimum value of the directional stiffness ratio with hardening shown in Fig. 2.5, hardening serves to diminish the softening-like behavior exhibited by nonassociative models. In fact, there exists a critical amount of hardening necessary to eliminate the possibility of attaining a negative value for the plastic directional stiffness, which in turn eliminates the possibility of localization. As would be expected, the figure shows that strain softening serves to increase the softening behavior of a nonassociative model (the minimum value of the directional stiffness ratio decreases with strain softening).

As shown in Fig. 2.5, the maximum value of the directional stiffness ratio increases when the model includes softening. This means that the spurious stiffening caused by nonassociative models is exacerbated by softening. Therefore, softening would be expected to exacerbate the Sandler-Rubin instability. Hardening serves to slightly decrease the maximum value of the directional stiffness ratio. Therefore, hardening would be expected to ameliorate the Sandler-Rubin instability.

Figure 2.6 shows numerical solutions to the case study problem with hardening and softening. For reference, the perfectly-plastic (nonhardening) solution is also shown with dashed lines. As suggested by the increase in the maximum value of the directional stiffness ratio with softening shown in Fig. 2.5, the plastic wave speed has increased as compared to the nonhardening solution. With this increase in plastic

wave speed with softening, the degree of instability has also increased. In contrast, the solution with hardening shows a decrease in the plastic wave speed, and a decrease in the degree of instability. It can be shown that only as the hardening modulus approaches infinity does the plastic wave speed approach the elastic wave speed. In contrast to what was found with the localization instability, there is no critical amount of hardening or softening that eliminates the Sandler-Rubin instability.

Stoughton [38] has asserted that the Sandler-Rubin instability cannot exist if the plastic tangent modulus is not constant to first order. The basis for this assertion is that if nonconstant wave speeds are substituted into the Sandler-Rubin solution, the resulting expressions fail to satisfy the governing equations. However, as discussed by Pučik et al. [16], this does not mean that the Sandler-Rubin instability cannot exist if the wave speed is not constant —it simply means that the Sandler-Rubin analytical solution was limited to the special case of a constant wave speed. Accordingly there is no reason to believe that such a solution should be expected to apply to a nonconstant wave speed.

Stoughton defines several classes of plasticity models that do not result in a constant plastic tangent modulus, and therefore were claimed not to admit the Sandler-Rubin instability. One class of models that has this attribute is any model with nonlinear hardening. To illustrate that such a model does admit the instability, the case study problem was solved using the same linear Drucker-Prager model with the following nonlinear hardening yield function:

$$f = \sqrt{J_2} + \beta I_1 - k_{\mathrm{limit}} - (k_o - k_{\mathrm{limit}})e^{-z/z_{\mathrm{ref}}} \tag{2.6}$$

where k_{limit} is the maximum value of the yield strength, z is the cumulative equivalent plastic strain, and z_{ref} is a parameter that controls the rate at which the maximum yield strength is approached.

The nonlinear hardening parameters were chosen to be $k_{\mathrm{limit}} = 10$ MPa, and $z_{\mathrm{ref}} = 0.001$. The left-hand side of Fig. 2.7 shows a plot of axial stress versus axial strain for a uniaxial stress loading path with the nonlinear hardening model and the chosen parameter values. As the plot clearly indicates, the plastic tangent modulus (and thus the plastic wave speed), is continually changing with plastic loading. The

stress histories found using this model and a mesh resolution of $\Delta x = 0.125$ m are shown in Fig. 2.7. As the stress histories indicate, the instability remains even with nonlinear hardening, thus providing a counter example contradicting Stoughton's conclusions. Furthermore, the solution also does not converge with mesh refinement, indicating that the governing equations remain ill-posed for this case.

2.5.2   Incrementally Nonlinear Plasticity

While a large body of evidence suggests that the use of an associative flow rule is inappropriate for many materials [7, 4], the physically implausible instability illustrated above is inherent in all nonassociative flow rules. Since both an associative and nonassociative flow rule seem to be at odds with experimental data, we ought to question the validity of assumptions upon which both of these flow rules rest.

One such assumption is the existence of a regular flow rule. A regular flow rule is defined as one for which the direction of the plastic strain rate is independent of the direction of the strain rate itself. Of the very few studies to investigate the validity of this assumption, most have cast considerable doubt on the validity of a regular flow rule for general loading conditions [42, 43, 44]. Several incrementally nonlinear flow rules have been proposed in the literature [45, 46, 47, 48, 44]. One of these, the "Extended Flow Rule" (EFR) proposed by Hashiguchi [45], is investigated as a possible alternative to the use of a regular flow rule. This flow rule was chosen since it may be easily incorporated within the basic framework of classical plasticity. The only difference is that the direction of the plastic strain rate is permitted to change based on the direction of the strain rate tensor. For this flow rule, the direction of the plastic strain rate $\boldsymbol{M}$ is given by:

$$\boldsymbol{M} = \hat{\boldsymbol{N}} \, \|\dot{\boldsymbol{e}}^*\| + P_t^v \dot{e}_v \boldsymbol{I} + P_t^* \dot{\boldsymbol{e}}^* \qquad (2.7)$$

where $\hat{\boldsymbol{N}}$ is the unit normal to the yield surface, $\|:\|$ represents the Euclidean norm of its argument, $\dot{\boldsymbol{e}}^*$ is the deviatoric part of the strain rate tensor, $\dot{e}_v$ is the volumetric part of the strain rate tensor, $\boldsymbol{I}$ is the identity tensor, and P_t^v and P_t^* are fitting parameters that control the degree to which the direction of plastic strain rate will be influenced by the direction of the strain rate tensor. Taking P_t^v and P_t^* to be zero

would result in a regular, associative flow rule. By selecting nonzero values for one or both of these parameters the constitutive model may be calibrated such that it accurately predicts the volumetric strain observed in triaxial compression tests, while at the same time preventing the Sandler-Rubin instability by precluding the plastic wave speed from exceeding the elastic wave speed for any loading direction.

This flow rule was implemented using the Drucker-Prager constitutive model used in the example problem, with $P_t^v = 0.5$ and $P_t^* = 0$. With these values, a triaxial compression test will result in very little volumetric plastic strain, as would be expected from a triaxial compression test on a rock-like material. The directional stiffness ratio for this model, and a perfectly plastic Drucker-Prager yield function, is shown on the left-hand side of Fig. 2.8. For all loading directions, the directional stiffness ratio is less than one, indicating that no spurious stiffening is possible with this flow rule. The right-hand portion of this figure shows the stress histories for the case study problem with this flow rule. As expected by the boundedness of the directional stiffness ratio, no instability is evident with this flow rule. In fact the stress wave dissipates, rather than grows, as it propagates. Like a nonassociative flow rule, there are loading directions for which the directional stiffness ratio is negative. This means that this flow rule and choice of parameters will still admit localization for some loading directions. As mentioned in Section 2.2, the ability to localize while in the hardening regime is a desirable feature of a plasticity model.

While eliminating the Sandler-Rubin instability, being capable of matching triaxial compression data, and admitting the localization instability, such flow rules have undergone relatively little validation. Since an incrementally nonlinear flow rule is capable of exactly duplicating the triaxial compression response of a standard nonassociative model, triaxial compression tests alone will not validate or invalidate the EFR. The experimental measurements necessary to validate an incrementally nonlinear model are not straightforward. Additional data that measure the plastic strain increments resulting from a variety of loading directions would be necessary to determine if the EFR is in fact valid. As discussed in our concluding remarks, such measurements may be critical to resolving the problems discussed in this paper, but performing such tests introduces irreducible uncertainty in the data. In the absence

of such data, it would seem most prudent to choose a flow rule such as the EFR, which disallows any nonphysical instabilities and can be fit to existing data.

2.5.3   Rate-dependent Plasticity

In this section, we consider the effect of rate dependency on the existence and characteristics of the Sandler-Rubin instability. In their original work, Sandler and Rubin [31] suggested that rate dependence might eliminate the nonphysical behavior caused by nonassociative plastic flow. The context of their suggestion was a discussion of the impacts of the Sandler Rubin instability for quasi-static problems. The instability is inherently dynamic, but it is rational to demand that the quasi-static solution be admissible only if it is stable under infinitesimal dynamic perturbations. The conclusion is that if a nonassociative flow rule is inappropriate for dynamic problems involving infinitesimal perturbations, then it also ought to be rejected for quasi-static problems. If rate dependence were shown to be capable of eliminating the instability for dynamic problems, then there would be no concern in using current rate-independent plasticity models for quasi-static problems.

With this motivation, the case study problem discussed above was solved using a rate-dependent generalized Duvaut-Lions model. The generalized Duvaut-Lions model is an "overstress" model, meaning that, under high-rate loading, it allows the stress state to fall outside the yield surface. The "overstress" is quantified by:

$$\boldsymbol{\sigma}^{\text{over}} = \boldsymbol{\sigma} - \boldsymbol{\sigma}^{\text{qs}} \tag{2.8}$$

where $\boldsymbol{\sigma}^{\text{qs}}$ is the corresponding quasi-static stress state. The strain rate $\dot{\boldsymbol{\epsilon}}$ is additively decomposed into elastic $\dot{\boldsymbol{\epsilon}}^{e}$ and viscoplastic $\dot{\boldsymbol{\epsilon}}^{\text{vp}}$ parts:

$$\dot{\boldsymbol{\epsilon}} = \dot{\boldsymbol{\epsilon}}^{e} + \dot{\boldsymbol{\epsilon}}^{\text{vp}} \tag{2.9}$$

The elastic strain rate is defined to be the same as in rate-independent theory. The viscoplastic strain rate is governed by:

$$\dot{\boldsymbol{\epsilon}}^{\text{vp}} = \frac{1}{\tau_{\text{mat}}} \mathbb{C}^{-1} {:} \boldsymbol{\sigma}^{\text{over}} \tag{2.10}$$

where τ_{mat} is the plastic relaxation time, and $\mathbb{C}^{-1}$ is the inverse of the elastic tangent stiffness tensor (elastic tangent compliance tensor). The basis for this type of model

is that plastic deformation requires a finite amount of time to develop. The time scale associated with plastic deformation is quantified by τ_{mat}. For a detailed description of this model see the book chapter by Brannon [2]. For rate-dependent models it is convenient to use the nondimensional Deborah number (De) to describe the loading rate. The Deborah number is defined as:

$$\mathrm{De} = \frac{\tau_{\mathrm{mat}}}{\tau_{\mathrm{load}}} \tag{2.11}$$

where τ_{load} is a time scale associated with the loading. A large De indicates that the loading time scale is short compared to the material relaxation time scale, which would produce an elasticity-dominated response. A small De indicates that the loading time scale is long compared to the material relaxation time scale, which would produce a plasticity-dominated response. In the limit as $\mathrm{De} \to 0$, a viscoplastic material model would predict a material response similar to a rate-independent model. In the limit as $\mathrm{De} \to \infty$, a viscoplastic material model would predict a response that is purely elastic.

Figure 2.9 shows a series of plots of the stress history at various locations in the problem domain using several values of De. As discussed above, for low De, the material behavior would be expected to be similar to the rate-independent response. However, for this case study problem the solution is nonunique across the peak of the wave. This fact allows the solution in this region to change dramatically with even small changes in the material response. This is evident in the stress histories for $\mathrm{De} = 0.01$ shown in Fig. 2.9. As would be expected, the head and tail of the wave are propagating with essentially the same speed as with the rate-independent solution (dashed line). However, the numerical solution across the peak of the wave is dramatically different than with the rate-independent model, and has become much more unstable. Again, this should not be cause for concern since no unique solution exists for this region of (x, t) space. As discussed in Section 2.3, the only constraints on the solution in this region are that the stress rate be greater than or equal to zero, and that the wave speed be greater than the elastic wave speed and less than the plastic wave speed. The numerical solution for $\mathrm{De} = 0.01$ shown in Fig. 2.9 satisfies both of these constraints.

When the relaxation time is nearly the same as the loading rate, the material behavior would be expected to become more elastic. This can be seen in the stress history plots for De = 1 shown in Fig. 2.9. For this solution the head and tail of the wave are diverging at a much lower rate, and are propagating with a wave speed that lies between the elastic and plastic wave speeds. Because the actual stress state can transiently lie outside the yield surface with the viscoplasticity formulation used, the viscoplastic strain rate can be nonzero even when the quasi-static stress state is within the yield surface. After the quasi-static stress state enters the yield surface, the overstress will exponentially decay to zero so that the actual stress state will approach the quasi-static stress state as the material is unloaded. The rate at which this approach occurs depends upon the relaxation time. Therefore, when the relaxation time is of the same order as the loading rate, a large part of the tail of the wave may still be undergoing viscoplastic deformation, even though the quasi-static stress state is within the yield surface. This is why the tail of the wave becomes increasingly dispersed as De increases as seen in Fig. 2.9. This also causes an increasing portion of the tail of the wave to be in a viscoplastic state as De increases. This also reduces the rate at which the head and tail of the wave diverge at high De, thereby decreasing the degree of instability in the solution. Also, for the mesh resolutions considered ($\Delta x = 2$ m to $\Delta x = 0.125$ m), the numerical solutions for De > 5 seemed to converge to a unique solution, although the instability remains.

2.5.4   Nonlocal Plasticity

As was mentioned in Section 2.2, there are two known material instabilities that may arise with the use of nonassociative plasticity models: a localization instability and the Sandler-Rubin instability. In the case of localization, the instability is an actual phenomenon that a realistic model ought to admit. Nonetheless, to achieve unique solutions to localization problems, some modification of the model is required to regularize the governing equations. Two commonly used approaches to regularizing localization problems are nonlocal plasticity and gradient plasticity. Both of these modifications to traditional plasticity theory cause wave propagation to become dispersive, which means that waves of different frequencies propagate at different

velocities. Dispersive wave propagation behavior has been shown to be critical to allowing these types of models to lead to mesh-independent numerical solutions to localization problems [49, 50].

Since nonlocal theory has proven useful to improve other aspects of plasticity theory (the ill-posedness due to localization), and since nonlocal theory predicts nonclassical wave propagation behavior, it seems prudent to investigate its effect upon the Sandler-Rubin instability, which inherently involves wave propagation. In this section, we investigate the effect of nonlocal plasticity and the resulting dispersive wave propagation behavior on the Sandler-Rubin instability. This is done by solving our case study problem using an integral-type overlocal plasticity model as described by Stromberg and Ristinmaa [51]. An overlocal model includes both local hardening/softening and nonlocal hardening/softening. The overlocal Drucker-Prager yield function is given by:

$$f = \sqrt{J_2} + \beta I_1 - k_o - (1 - m)\eta - m\zeta \qquad (2.12)$$

where η is the local hardening/softening function, ζ is the nonlocal hardening/softening function, and m is the overlocal parameter. For $m = 0$, a purely local model is obtained, and for $m = 1$ a purely nonlocal model is obtained. As discussed by both Stromberg and Ristinmaa [51] as well as Di Luzio and Bazant [50], the best localization limiting properties are obtained with the overlocal choice, $m > 1$. In this paper we use $m = 2$. The hardening/softening functions evolve according to:

$$\dot{\eta}(\boldsymbol{x}) = h\dot{\lambda}(\boldsymbol{x}) \qquad (2.13)$$

where $\dot{\lambda}$ is the magnitude of the plastic strain rate tensor (plastic multiplier), and

$$\dot{\zeta}(\boldsymbol{x}) = \frac{h}{V_\alpha} \int_\Omega \alpha(\boldsymbol{x} - \boldsymbol{s})\dot{\lambda}(\boldsymbol{s})dV \qquad (2.14)$$

where $\boldsymbol{x}$ is the position vector of a given material particle, h is the hardening/softening modulus (here taken to be a constant material parameter), $V_\alpha = \int_\Omega \alpha(\boldsymbol{s})dV$, and $\alpha(\boldsymbol{x})$ is the nonlocal weighting function, here chosen to be the Gaussian distribution function given by:

$$\alpha(\boldsymbol{x}) = \mathrm{Exp}\left[(-k\left\|\boldsymbol{x}\right\|/L)^2\right] \qquad (2.15)$$

where $k = (6\sqrt{\pi})^{\frac{1}{3}}$, and L is the nonlocal length scale. With the nonlocal term, the yield function at each material point becomes coupled with all material points within the support of $\alpha(\boldsymbol{x})$. To solve this coupled set of equations, a new fixed-point iteration scheme, which is described in Chapter 4, was developed and implemented into the MPM solution procedure.

A perturbation analysis technique described by Di Luzio and Bazant [50] was adapted to solve for the frequency-dependent wave propagation velocity for the uniaxial strain wave propagation problem in this paper. The left-hand side of Fig. 2.10 shows the resulting wave propagation velocity versus frequency for the nonlocal Drucker-Prager model. Unlike the dispersion relations for localization problems reported in the literature, which focused on low values of the directional stiffness ratio, with the overlocal Drucker-Prager model at high directional stiffness ratios, no localization occurs. Hence there is no critical wave frequency at which the propagation speed is zero. This is due to the over-stiffening behavior of the nonassociative model for the loading directions involved in this problem. The wave propagation velocity is bounded by the purely local softening wave speed (upper bound) and by the purely local wave speed (lower bound). This is because with low frequencies (and therefore small gradients) the nonlocal average of the plastic strain approaches the local value, so the nonlocal model results in little change as compared to a purely local softening model. For high frequency waves, the nonlocal average for a material particle will be much less than the local value since neighboring "elastic" particles, whose plastic strain rate tensor is zero, are included in the average. Therefore, for high frequencies, the local term of the overlocal hardening/softening dominates, and the response approaches that of a local hardening model.

The case study was solved using a nonlocal length scale of $L = 1.0$m. The internal length scale is tied to the length scale associated with a critical material microstructure. The critical material length scale depends upon the length scale associated with the problem geometry and the wave length of the solution. This case study problem is meant to represent a stress wave propagating through geologic strata. For the length scales involved and the frequency of the solution, the critical

material structure driving the nonlocal length scale would likely be the thickness of bedding planes or similar geologic structures. With this in mind a nonlocal length scale of one meter would be reasonable.

The right-hand side of Fig. 2.10 shows the stress histories at various locations in the problem domain using the overlocal model discussed above. For reference, the local softening solution is shown with a dashed line. Consistent with the dispersion plot in the same figure, the overlocal model has resulted in a reduction in the plastic wave speed relative to the local softening solution. Nevertheless the instability and nonuniqueness persist. As can be seen by the horizontal separation of the curves in Fig. 2.10, the difference in arrival time is greater for the secondary pulse than it is for the primary pulse. This is thought to be due to the higher frequency of the secondary pulse, which according to the dispersion relation for this problem results in a decrease in wave speed as compared to lower frequency waves.

From the dispersion relation and the overlocal case study solution, we conclude that a nonlocal plasticity model neither eliminates the Sandler-Rubin instability, nor the resulting ill-posedness.

2.6   Concluding Remarks

Of the models considered, only Hashiguchi's incrementally nonlinear extended flow rule (EFR) [45] was found to eliminate the Sandler-Rubin instability. The viscoplastic model considered here resulted in mesh-independent solutions for high loading rates, but the nonphysical instability was present for all loading rates considered. Both the instability and the mesh dependency of the numerical solution were observed with both linear and nonlinear hardening and softening. The fact that the instability persisted even with nonlinear hardening constitutes a counter example to Stoughton's assertion [38] that nonlinear hardening would preclude the instability. Hardening tended to diminish the instability, while softening tended to exacerbate it. The nonlocal plasticity solutions were very similar to the local plasticity solutions. Therefore, of the models considered here, the incrementally nonlinear EFR model is the only one that eliminates the instability while maintaining the desirable aspects of a nonassociative model.

As discussed in Section 2.5.2, Hashiguchi's EFR model introduces new material parameters that must be calibrated to a material of interest. To choose these parameters for a given material, the plastic strain increment must be measured for several loading directions. To measure the plastic strain increments, laboratory tests must include unloading increments. Furthermore, to measure these increments at the same material state for a different loading direction requires nonproportional loading. A limited amount of such data is available in the literature, and collecting such data is complicated by the loading-history dependent nature of plastic loading [52].

Measuring the components of any tensor (in our case the tangent stiffness) requires measuring the response to more than one loading direction. In measuring the plastic strain increment for one loading direction, however, the material is permanently altered, making it impossible to know how the material would have responded to a different loading direction from the same initial state. Any further loading of the material with a loading increment in a different direction begins at a different material state. Therefore it is impossible to measure the tangent stiffness in the laboratory with certainty. Stoughton [33] pointed out a few additional problems with making such measurements. Specifically he mentioned that many materials of interest do not exhibit a "sharp" yield point, but instead the material gradually transitions from elastic to elastic/plastic deformation, making detection of the onset of yield difficult. Several techniques have been used to ameliorate this problem, each with its own drawbacks [42, 43]. A new technique that seeks to overcome some of these problems is presented in Chapter 3.

The flow rule validation studies from the sheet metal forming community [11, 10, 34] have performed a best-fit parameterization of associative and nonassociative regular flow rule models to a subset of their experimental data. The models were then used to generate predictions for other experimental data that were not used for model calibration. As mentioned previously, these studies have shown that a nonassociative flow rule is better able to match the experimental data. Although these tests were performed for a wide variety of loading directions, none of these tests explicitly measured the plastic strain increments by including unloading increments. These and other tests already mentioned do provide a compelling case against an

associative flow rule, but they do not provide any evidence for or against the validity of a regular flow rule.

To our knowledge, no study has conclusively validated or invalidated the existence of a regular flow rule. Therefore, the validity of the incrementally nonlinear approach is a critical topic for future experimental work. It is suggested that future validation efforts include incrementally nonlinear models as a possible alternative to traditional regular flow rules. Until such experimental evidence becomes available, it seems prudent to choose a model that fits known data while at the same time disallowing the nonphysical instabilities evident in traditional nonassociative plasticity. Therefore analysts may consider adopting an incrementally nonlinear approach if an analysis involves loading paths in the directions which could potentially excite the Sandler-Rubin instability.
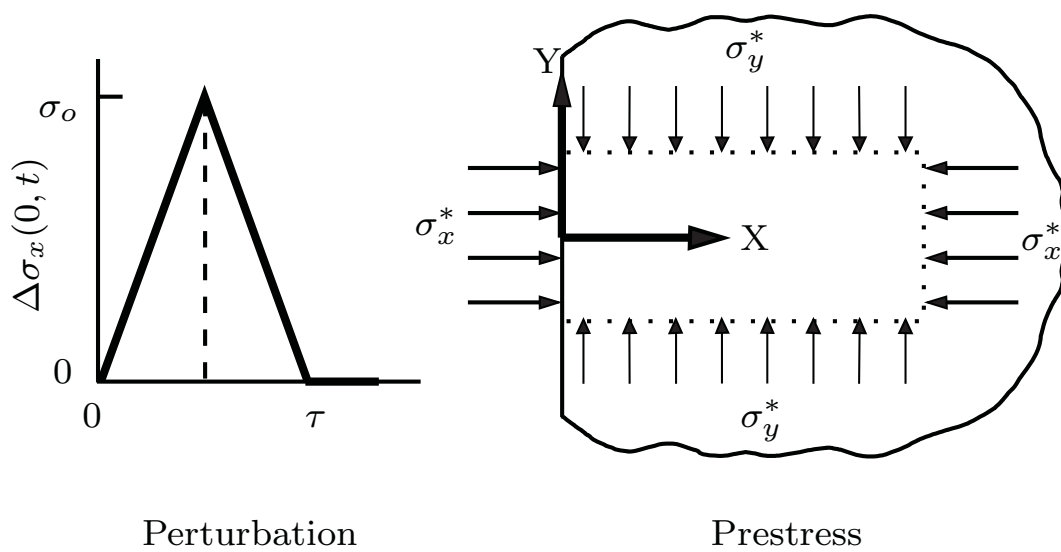
Figure 2.1. Geometry and loading for the case study problem.
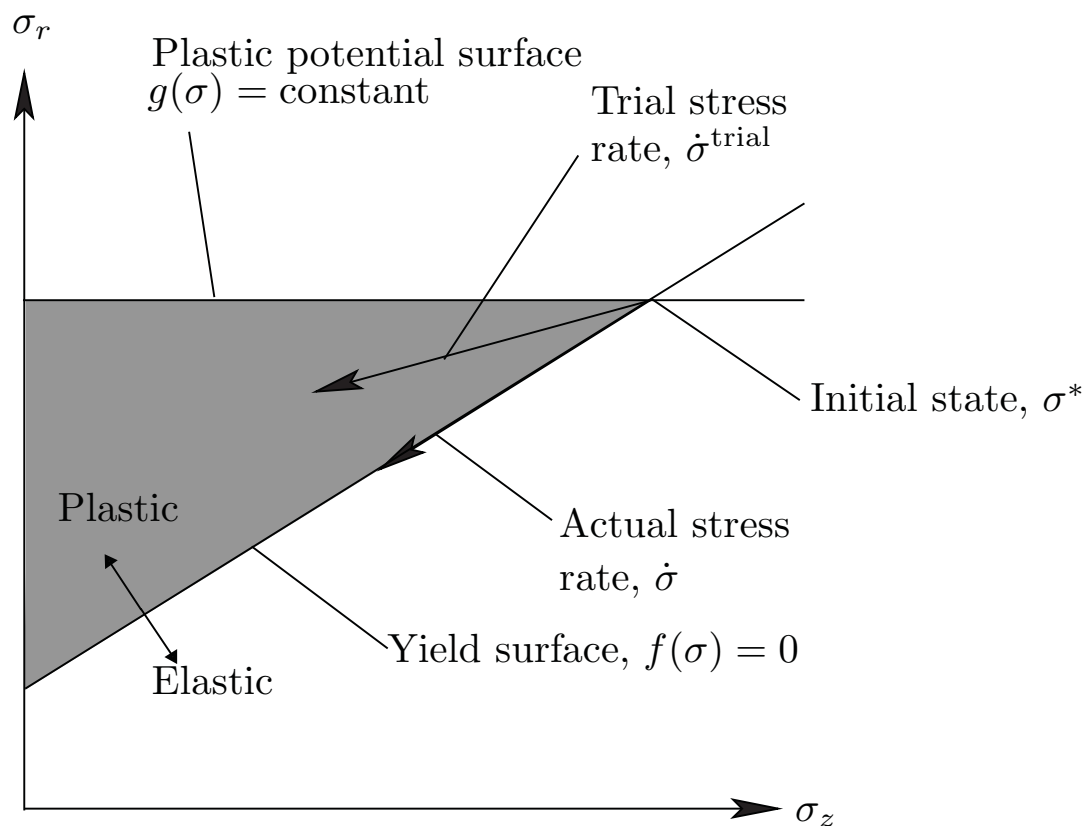
Figure 2.2. Illustration of the initial state with the yield surface $f(\boldsymbol{\sigma}) = 0$ and plastic flow potential iso-surface $g(\boldsymbol{\sigma})$ shown in Lode coordinate space ($\sigma_r = \|\boldsymbol{S}\|$, $\sigma_z = \frac{1}{\sqrt{3}}\text{Tr}(\boldsymbol{\sigma})$). $\hat{\boldsymbol{M}}$ is the direction of the plastic strain rate, $\dot{\boldsymbol{\sigma}}^{\text{trial}}$ is the stress rate, and $\dot{\boldsymbol{\sigma}}$ is the actual stress rate.
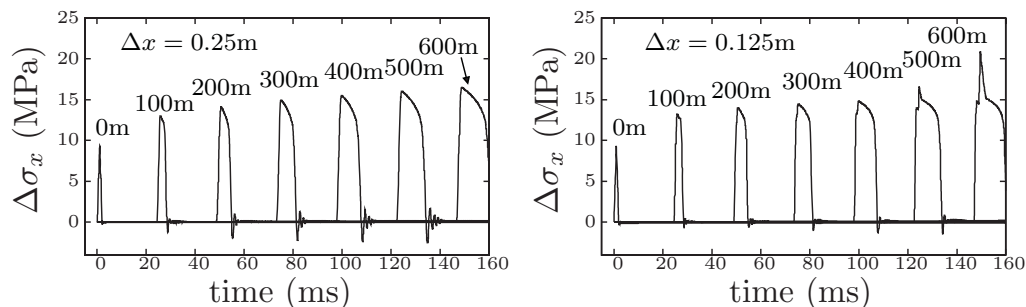
Figure 2.3. Stress histories at various locations throughout the problem domain using a local plasticity model, no hardening, and a mesh resolution of $\Delta x = 0.25\,\mathrm{m}$(left) and $\Delta x = 0.125\,\mathrm{m}$ (right). This result uses the MPM to independently reconfirm the existence of the Sandler-Rubin instability previously shown to exist using the FEM.
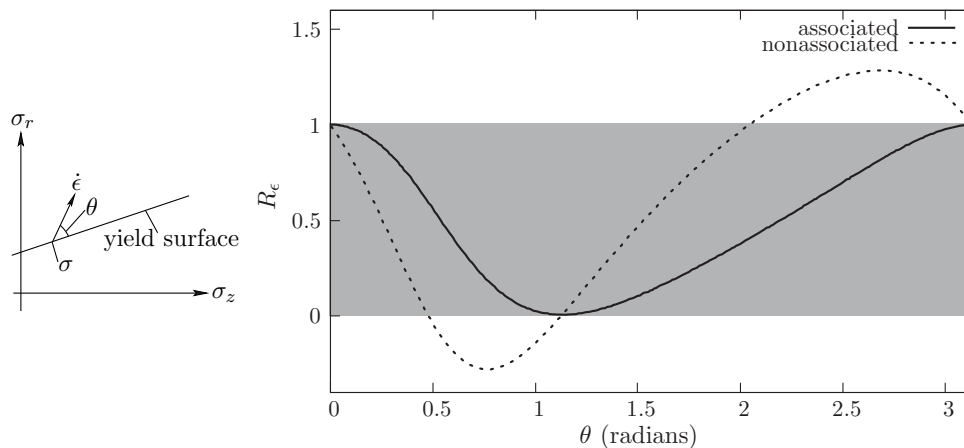
Figure 2.4. Directional stiffness ratio for nonhardening, associative and nonassociative linear Drucker-Prager models for all axisymmetric loading directions. $\sigma_z = -\frac{1}{\sqrt{3}}\mathrm{Tr}(\boldsymbol{\sigma})$ and $\sigma_r = \left\|\boldsymbol{\sigma} - \frac{1}{3}\mathrm{Tr}(\boldsymbol{\sigma})\right\|$
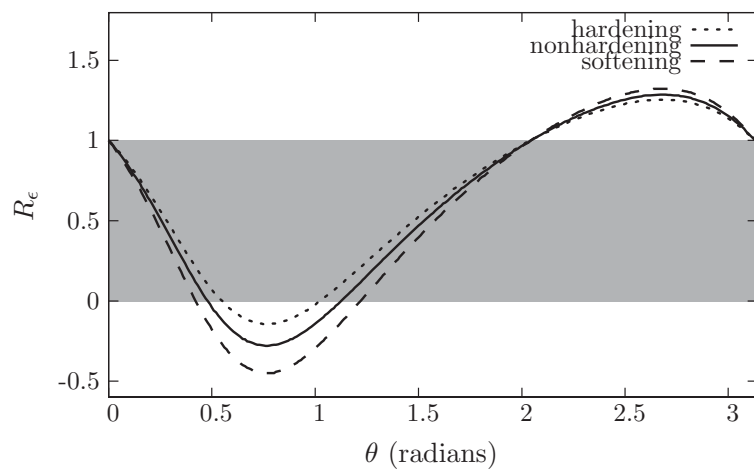
Figure 2.5. Directional stiffness ratio for a nonassociative model with softening, nonhardening (perfect plasticity) and hardening
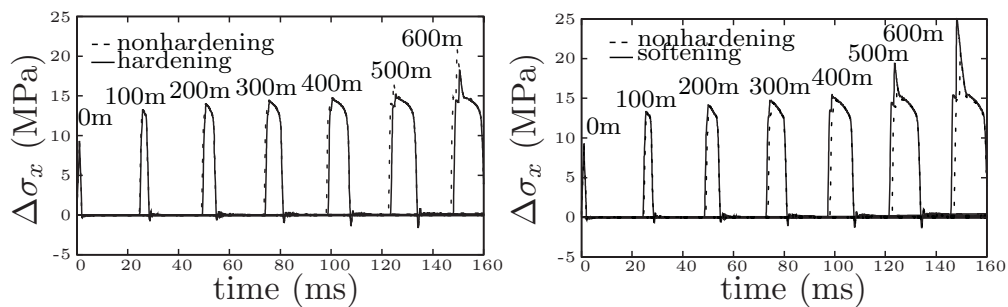
Figure 2.6. Stress histories for the numerical solution using hardening (left) and softening (right)
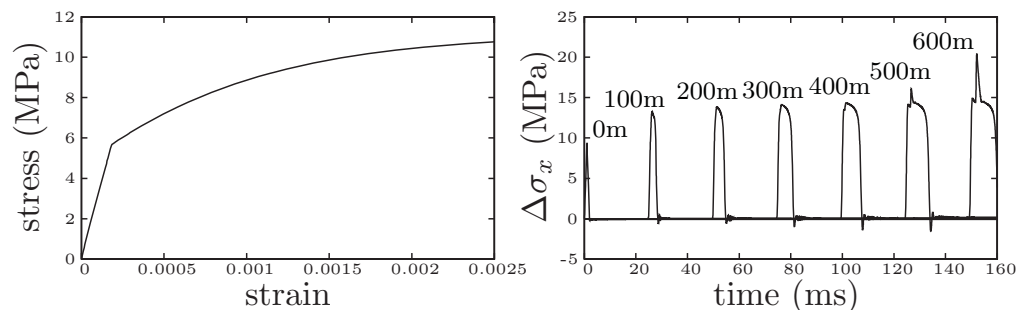
Figure 2.7. Uniaxial stress versus strain plot for the nonlinear hardening model (left), and stress histories for the numerical solution to the case study problem using the nonlinear hardening model (right)
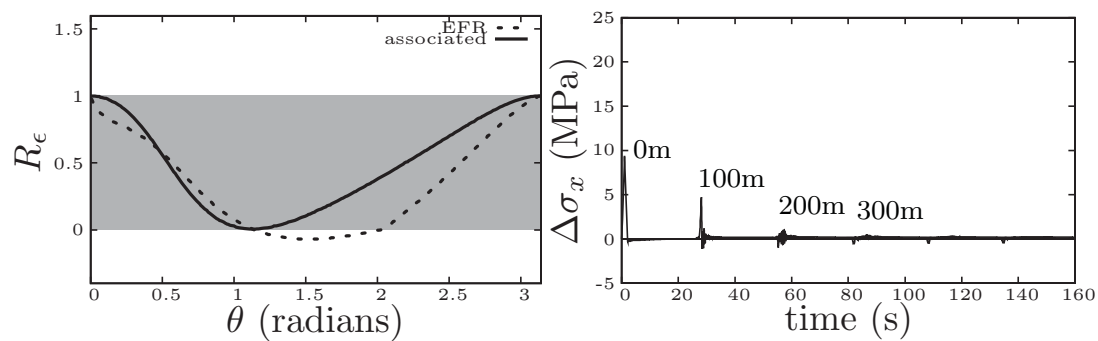
Figure 2.8. Illustration of the effect of the extended flow rule (EFR) on the Sandler-Rubin instability. Left: The directional stiffness with the EFR for all axisymmetric directions. The stiffness is never greater than the elastic, but the stiffness is negative for some directions. Right: Stress histories every 100 meters through the problem domain using the extended flow rule (EFR) with $P_v = 0.5$.
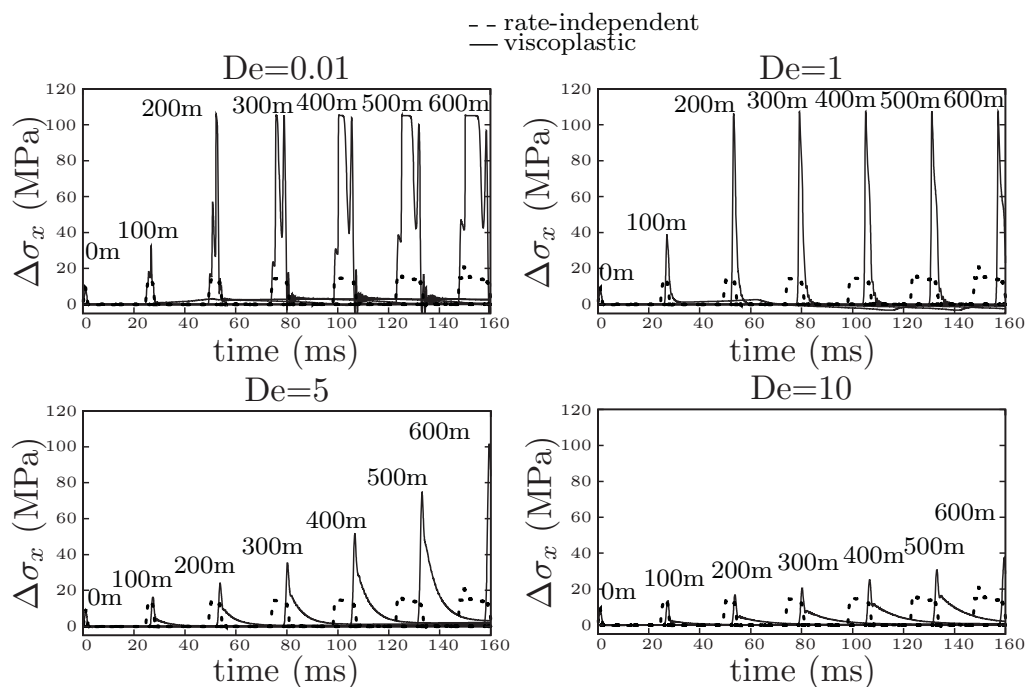
Figure 2.9. Stress histories for a Duvaut-Lions viscoplasticity model, with $\Delta x = 0.125$m, and De $= 0.01$ (top left), De $= 1$ (top right), De $= 5$ (bottom left), and De $= 10$ (bottom right).
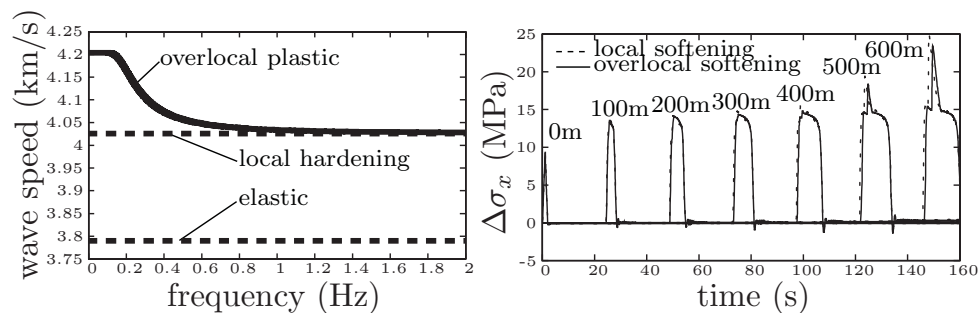
Figure 2.10. A plot of the frequency-dependent wave propagation velocity for the case study problem with an overlocal plasticity model, with the elastic and local hardening wave speeds shown for reference (left). Stress histories using an overlocal plasticity model with a nonlocal length scale of 1m and a mesh resolution of 0.125m (right).

CHAPTER 3

EXPERIMENTAL VALIDATION OF
INCREMENTAL NONLINEARITY

3.1   Abstract

A new experimental method and data analysis technique for directly measuring the incremental stress-strain response of a material is described. Using this technique it is possible to measure the incremental response to a variety of loading directions from a single material sample. This eliminates the need to fabricate a series of identical specimens as with existing stress probe techniques. A rigorous mathematical framework for fitting classical theories to the data, and quantifying the error, is provided. This methodology is used to measure the incremental response of a series of aluminum 6061-T0 specimens, and to evaluate the validity of classical theories for this material. The results suggest that there is some degree of incremental nonlinearity (i.e., the direction of the inelastic strain increment depends on the total strain increment direction).

3.2   Introduction

The stress-strain relationship for most materials is nonlinear and path dependent. For this reason the stress state at time t is, in general, a functional of the entire loading history:

$$\boldsymbol{\sigma}(t) = \mathcal{F}[\boldsymbol{\epsilon}(\tau), \gamma(\tau); 0 \leq \tau \leq t] \qquad (3.1)$$

where $\boldsymbol{\sigma}$ is the stress tensor, $\boldsymbol{\epsilon}$ is the strain tensor, and γ represents other variables such as temperature that might alter the mechanical behavior of the material. Since formulating a constitutive model using nonlinear functionals would generally be intractable, a useful simplification is to express the stress rate tensor, $\dot{\boldsymbol{\sigma}}$, as a function

of the strain rate tensor, $\dot{\boldsymbol{\epsilon}}$, the stress tensor, and a set of internal state variables, denoted collectively as ξ, which account for previous loading history:

$$\dot{\boldsymbol{\sigma}}(t) = \mathcal{G}[\dot{\boldsymbol{\epsilon}}(t), \boldsymbol{\sigma}(t), \xi(t)] \tag{3.2}$$

In general, $\mathcal{G}$ is a nonlinear tensor-valued function. Again due to the difficulty of working with nonlinear tensor-valued functions, further assumptions are often introduced to simplify Eq. (3.2). One such assumption is rate independence. If material response is assumed to be independent of the loading rate, then the function $\mathcal{G}$ in Eq. (3.2) is a homogeneous function of degree one in the variable $\dot{\boldsymbol{\epsilon}}$. Euler's theorem for homogeneous functions then allows Eq. (3.2) to be written as

$$\dot{\boldsymbol{\sigma}}(t) = \mathbb{H}[\hat{\dot{\boldsymbol{\epsilon}}}, \boldsymbol{\sigma}(t), \xi(t)]{:}\dot{\boldsymbol{\epsilon}} \tag{3.3}$$

where $\mathbb{H} = \frac{\partial \mathcal{G}}{\partial \dot{\boldsymbol{\epsilon}}(t)}$ is a fourth-order tensor called the tangent stiffness, and $\hat{\dot{\boldsymbol{\epsilon}}}$ is a unit tensor in the direction of the strain rate tensor. Many assumptions have been proposed that further simplify Eq. (3.3). The assumptions of interest in this paper regard the degree to which the tangent stiffness tensor $\mathbb{H}$ depends on the loading direction $\hat{\dot{\boldsymbol{\epsilon}}}$. For example, if the material response is assumed to be nonlinear elastic, the tangent stiffness tensor is independent of the loading direction. This means that the relationship between the stress rate, $\dot{\boldsymbol{\sigma}}$, and the strain rate, $\dot{\boldsymbol{\epsilon}}$, is linear, and hence is called an incrementally linear relationship. For this case, Eq. (3.3) can be reduced to

$$\dot{\boldsymbol{\sigma}} = \mathbb{C}(\boldsymbol{\sigma}){:}\dot{\boldsymbol{\epsilon}} \tag{3.4}$$

where $\mathbb{C}$ is the fourth-order elastic tangent stiffness tensor. This result shows the stress increment to be linear with respect to the strain increment, and does not imply Hooke's law in which stress is linear with respect to strain. Linear elasticity corresponds to the the tangent stiffness being independent of $\boldsymbol{\sigma}$.

For classical rate-independent plasticity theories, a loading increment is considered to be elastic if $f(\boldsymbol{\sigma}(t), \xi(t)) < 0$, where f is a scalar function called the yield function. The set of stress states for which $f = 0$ defines the yield surface. When a stress state has reached the yield surface, loading directions for which $\hat{\boldsymbol{N}}{:}\mathbb{C}{:}\hat{\dot{\boldsymbol{\epsilon}}} > 0$ represent plastic loading, and the directions for which $\hat{\boldsymbol{N}}{:}\mathbb{C}{:}\hat{\dot{\boldsymbol{\epsilon}}} < 0$ represent elastic unloading.

These regions of the loading space are referred to as tensorial zones. Figure 3.2 illustrates both a classical incrementally bilinear response, and a general nonlinear response using a Gudehus strain response diagram. The results from this chapter will be presented using Gudehus diagrams in Section 3.6.

Within each tensorial zone there exists a tangent stiffness tensor, each independent of the loading direction. Thus, elasticity theory defines a single tensorial zone, and classical plasticity defines two tensorial zones. These correspond to an incrementally linear and bilinear constitutive relation, respectively. The validity of the incrementally bilinear constitutive relationship of classical plasticity theory rests on the assumption of the existence of a regular flow rule. A regular flow rule means that the direction of the plastic strain rate is not a function of the loading direction. Two classes of regular flow rules exist: associative and nonassociative. The associative flow rule assumption uses the gradient of the yield function to fix the direction of the plastic strain rate.

The use of an associative flow rule has been shown to overpredict plastic volume changes for materials with a pressure-dependent yield strength [7, 4]. This led to the adoption of a nonassociative flow rule, where the direction of the plastic strain rate is found from the gradient of a function, often called the plastic potential, that is different from the yield function. Nonassociative flow rules have been shown to accurately predict plastic volume changes under monotonic triaxial compression load paths [7, 4]. However, adoption of a nonassociative flow rule has also been shown to lead to physically unjustifiable instability, as well as nonuniqueness in the governing equations for certain boundary value problems [31, 32, 16, 15, 53, 54, 55]. As discussed in Sections 1.4.2 and 2.5.1, other studies have used experimental data [4] or theoretical analysis [37, 38] to counter arguments against nonassociativity.

All of the aforementioned studies assume the validity of a regular flow rule, that is, they begin with the premise that there exist only two tensorial zones. Despite widespread acceptance, relatively little validation work has been done to justify the use of a regular flow rule. Recently, however, several such studies have been undertaken [56, 57, 43, 44]. These studies have used two basic approaches: computational and experimental. The computational techniques use the discrete element method (DEM) to model the response of granular materials to a variety of loading directions.

The experimental investigations have used a "stress probing" technique where a set of nominally identical samples are each loaded to a desired stress state along a specified path. Once at the desired state, each sample is loaded in a different direction, and the resulting strain response is measured. The advantage of the computational schemes is that it is possible to exactly duplicate a particular material state for several tests by simply using the same initial conditions for several simulations. In this way one can be sure that each stress-strain increment pair is measured at an identical material state and for an identical material. The drawback to these methods is that they rely on many unvalidated assumptions, as well as parameters that are not easily measured in the laboratory. For this reason, the results of the DEM studies are at best a qualitative measure of the possible response of real materials.

This paper outlines an alternative experimental technique that allows the constitutive relationship of Eq. (3.3) to be measured directly without introducing any a priori assumptions regarding incremental linearity. This method also eliminates the need for a set of identical material specimens. This approach is not only more convenient, but broadens the applicability of the stress probing technique to materials that have high levels of aleatory uncertainty.

3.3 Visualization of Nonlinear Transformations

The analysis of the laboratory experiments that will be described in Section 3.5 will make no assumptions that the material is incrementally linear or even isotropic. We will simply plot the strain increment (response) vectors resulting from stress increment (stimulus) vectors that are in various directions, but each of equal length. Because the stimulus vectors are all of equal length, plotting them joined at the tails produces a set of vectors whose tips form a circle, as illustrated in Fig. 3.1. Doing the same type of tail-to-tail plot for the response vectors allows direct visualization of the degree to which the transformation from stress increments to strain increments is linear. A necessary condition for a transformation to be linear is that the response envelope must form an ellipse, as in 3.1(b). This is not a sufficient condition, as seen in Fig. 3.1(d); a linear transform has the appearance of a uniform stretching

of the stimulus disk, possibly in combination with some rotation. An example of a more "ordinary" nonlinear transformation is shown in Fig. 3.1(c). Fig. 3.2 shows a Gudehus response envelope for a classical elastoplastic theory, which is incrementally bi-linear, as well as a more general incrementally nonlinear response envelope.

Incidentally, the plots in Fig. 3.1 are superior to Reynolds glyphs [58] because a Reynolds glyph fails to convey information about rotation and, as mentioned, it does not depict irregular vector distributions on the ellipse (or ellipsoid in 3D). Reynolds glyphs for stress-strain transformations are often referred to as "Gudehus" diagrams [59]. It is also important that all stimulus-response (for our case stress-strain) vectors be taken beginning at the same material state, which includes both the same stress state, as well as the same loading history. Loading history must be included in the definition of "material state" for plastic materials since inelastic loading can irreversibly alter the material. This makes it literally impossible to measure a strain response envelope for history-dependent materials with certainty. The experimental method in Section 3.4 and the data analysis technique in Section 3.5 describe a new technique that seeks to address the uncertainty in measuring the strain response envelope for history-dependent materials.

3.4   Experimental Methodology

Because of the history-dependent nature of plastic loading, obtaining multiple independent stress-strain increment measurements from the same initial material state is literally impossible. The act of making one such measurement can irreversibly alter the material and thus preclude knowing with certainty how the material would have responded to a different loading increment. To avoid this problem, most studies of this nature turn to computational methods, which allow exactly resetting the material state for probing in new directions. As discussed in Section 3.2, most experimental studies have sought to overcome this problem by preparing a set of nominally identical specimens, loading them each through identical load paths to the same reference state, and then applying a different loading increment to each specimen. To eliminate the need for "identical" samples, the method described in this report allows independent loading increments to be obtained at the same

material state from a single specimen using cyclically applied loading increments and an interpolation scheme.

This concept is illustrated in Fig. 3.3, where the cyclical load begins at an initial material state denoted by ψ_1. An incremental stress loading vector $d\sigma_A$ is then applied taking the material state to ψ_2. Then, a different stress loading vector $d\sigma_B$ is applied, taking the material state to ψ_3. Finally, the incremental loading vector $d\sigma_A$ is applied again, this time beginning from material state ψ_3. In each case, the incremental strain vector is measured. This results in three stress-strain incremental vector sets at three different material states. To find the tangent stiffness tensor at material state ψ_2, the strain response vector that would have resulted if loading vector $d\sigma_A$ had been applied at material state ψ_2 is needed. While this information is obviously not available, the strain response vectors corresponding to $d\sigma_A$ at states ψ_1 and ψ_3 are available. It is postulated that interpolation may be used with these two pieces of information to infer what the strain response *would have been* at material state ψ_2 if the loading vector $d\sigma_A$ had been applied at that point. In the limit of small loading increments this assumption is a reasonable approximation if the material changes in a continuous manner with the state variables. It amounts to approximating a hypersurface with a hyperplane between two points on the hypersurface. A one-dimensional analogy is approximating a continuous function with a straight line. As the end-points of the line become closer together, the approximation becomes increasingly good. Accordingly, the interpolation scheme is probably not appropriate in situations that include discontinuous changes in the material constitutive functions such as phase transformations.

The loading cycle used in this study is slightly more complicated than the one illustrated in Fig. 3.3. Rather than only two independent loading directions, eight have been used to allow better sampling of the material response to changes in the loading direction. Each loading leg also has been fully unloaded then reloaded before moving on to the next loading leg. The unloading allows the plastic strain increments to be inferred from the residual strain associated with each loading leg.

Four of the stress increment directions selected are anticipated to cause significant plastic flow. That is, for most pressure-sensitive nonporous plasticity models, these

four loading directions would be directed outward from the yield surface (increasing the stress deviator and/or decreasing the confining pressure). If a classical incrementally bilinear plasticity model is assumed, these loading directions allow the plastic tangent stiffness to be directly computed from measured stress-strain increments. We define a stress increment by:

$$\begin{aligned}\dot{\sigma}_z &= \dot{\Sigma}\cos\phi \\ \dot{\sigma}_r &= \dot{\Sigma}\sin\phi\end{aligned} \tag{3.5}$$

where $\dot{\Sigma}$ is the increment magnitude and ϕ is the angle formed between the stress increment and the hydrostatic compression axis. The stress measures σ_z and σ_r are the axial and radial Lode coordinates, which are measures of the hydrostatic and deviatoric stresses, respectively. The precise definitions of these stress measures will be given in Section 3.5. Using this description of an incremental loading vector given in Eq. (3.5), the four plastic loading legs labeled A, B, C and D are described in Table 3.1.

The direction of increment B consists simply of a reduction in the hydrostatic pressure with no change in the deviatoric stress. This direction is of particular interest since, as described in Chapter 2, for many nonassociative plasticity models it lies in the Sandler-Rubin wedge, which is the region between the yield surface and the isosurface of the plastic potential function.

Small increments ($\dot{\Sigma} = 100$ psi) were used in early tests, but the measurements had a low degree of repeatability since the "noise" from the measurements was of the same order of magnitude as the measurements themselves. The increments were progressively made larger until good repeatability was attained ($\dot{\Sigma} = 300$ psi).

Four additional stress increments were selected to be in the opposite direction of the four stress increments previously described. For most plasticity models these loading directions would be directed into the yield surface and therefore would be considered elastic unloading directions. If a traditional incrementally bilinear plasticity theory is assumed, these loading directions will allow the elastic tangent stiffness to be directly computed from measured stress-strain increments.

After each stress increment was applied, it was fully reversed before continuing with the next stress increment. This allows the plastic strain increment to be mea-

sured for each loading direction. The plastic strain increment was taken to be the strain increment that remained after the stress increment was fully reversed.

A triaxial compression fixture at Sandia National Laboratories was used to apply such a load path to a series of aluminum specimens. The specimens were all right-circular cylinders with a length-to-diameter ratio of 2:1 as recommended by ASTM D4534 for uniaxial and triaxial compression tests. The metal specimens were 1 inch in diameter extruded and annealed aluminum 6061-T0 cylinders that were cut to a length of 2 inches. Three strain gage pairs, each with a resolution of 10 microstrain, were then mounted at 120° intervals, with each gage pair being composed of an axial and lateral gage. As will be discussed below, it will be assumed that the specimens are at most transversely isotropic. The redundant gaging was used to confirm specimen alignment and to detect nonaxisymmetric deformation, which would be an indication of more general anisotropy or localization.

The results from three different tests will be discussed. Before conducting each test with a cyclical loading path, a specimen from the same batch of material was loaded through the same nominal loading path, but without the changes in loading direction. This was done to determine the point at which significant yielding was expected to begin. Based on this test, a new specimen was subjected to the same load path up to the point where significant plastic flow was expected, at which point the cyclical load path described above was performed. For each test, an initial hydrostatic confining stress was first applied to the specimen. Tests 1, 2, and 3 used an initial confining stress of 19.4 ksi, 18.8 ksi, and 18.4 ksi, respectively.

3.5   Data Analysis

As discussed in Section 3.4, only axisymmetric loading is considered in this study. It is assumed (and monitored through redundant gaging) that the specimens are at most transversely isotropic. With this assumption any second-order tensor in the analysis may be written in the form

$$[A] = \begin{bmatrix} A_A & 0 & 0 \\ 0 & A_L & 0 \\ 0 & 0 & A_L \end{bmatrix} \tag{3.6}$$

where the subscripts "A" and "L" refer to axial and lateral components, respectively. Equation (3.6) may be written as a linear combination of unit base tensors as

$$\begin{bmatrix} A_A & 0 & 0 \\ 0 & A_L & 0 \\ 0 & 0 & A_L \end{bmatrix} = (A_A) \begin{bmatrix} 1 & 0 & 0 \\ 0 & 0 & 0 \\ 0 & 0 & 0 \end{bmatrix} + \left(\sqrt{2}A_L\right) \frac{1}{\sqrt{2}} \begin{bmatrix} 0 & 0 & 0 \\ 0 & 1 & 0 \\ 0 & 0 & 1 \end{bmatrix} \qquad (3.7)$$

The normalization of the base tensors allows reducing the generally six-dimensional entity (a fully-populated symmetric second-order tensor [A]) to a simple two-dimensional vector having components A_A and $\sqrt{2}A_L$. The introduction of the $\sqrt{2}$ ensures that the ordinary magnitude of the vector

$$\begin{bmatrix} A_L \\ \sqrt{2}A_L \end{bmatrix} \qquad (3.8)$$

is the same as the magnitude of the corresponding tensor. For this reason, the two values (A_A and $\sqrt{2}A_L$) are said to be isomorphic to a six-dimensional tensor space. They are Euclidean coordinates within a two-dimensional plane that "cuts through" six-dimensional tensor space. With this reduction in dimension, the incremental equations of plasticity may be written as

$$\begin{bmatrix} \dot{\sigma}_A \\ \dot{\sigma}_L \end{bmatrix} = \begin{bmatrix} T_{AA} & T_{AL} \\ T_{LA} & T_{LL} \end{bmatrix} \begin{bmatrix} \dot{\epsilon}_A \\ \dot{\epsilon}_L \end{bmatrix} \qquad (3.9)$$

Whereas the above decomposition into axial and lateral components is most natural for the laboratory control, data analysis that aims to draw connections with conventional plasticity theories is better served by introducing a change of variables. For any axisymmetric tensor [A] defined by its isomorphic components (A_A and $\sqrt{2}A_L$), an alternative pair of isomorphic components, corresponding to an orthogonal basis rotation in the same two-dimensional space, is given by

$$\begin{bmatrix} A_z \\ A_r \end{bmatrix} = \frac{1}{\sqrt{3}} \begin{bmatrix} 1 & \sqrt{2} \\ \sqrt{2} & -1 \end{bmatrix} \begin{bmatrix} A_A \\ \sqrt{2}A_L \end{bmatrix} \qquad (3.10)$$

With this change of variables, Eq. (3.7) can be written as an equivalent expansion in terms of a different pair of unit base tensors as

$$\begin{bmatrix} A_A & 0 & 0 \\ 0 & A_L & 0 \\ 0 & 0 & A_L \end{bmatrix} = (A_z) \frac{1}{\sqrt{3}} \begin{bmatrix} 1 & 0 & 0 \\ 0 & 1 & 0 \\ 0 & 0 & 1 \end{bmatrix} + (A_r) \frac{1}{\sqrt{6}} \begin{bmatrix} 2 & 0 & 0 \\ 0 & -1 & 0 \\ 0 & 0 & -1 \end{bmatrix} \qquad (3.11)$$

which illustrates that these two alternative coordinates decompose axisymmetric tensors into their isotropic and deviatoric parts.

These alternative axisymmetric measures are subscripted "r" and "z" because they can be shown to correspond to the cylindrical coordinates that are naturally implied in the symmetry of common yield surfaces about the [111] axis (see, for example, [60]). For triaxial compression loading, the angular coordinate, called the Lode angle, is fixed on the compressive meridian. Therefore, because z-r Lode coordinates are isomorphic to stress space, all plots in z-r stress space are geometrically accurate depictions of a "side view" of the yield surfaces as plotted in principal stress space (i.e., they possess the same lengths and angles). It is this feature, as well as inheritance of tensor properties, such as symmetries and eigensystems of the tangent tensor, that recommends isomorphic tensor measures over perhaps more (initially) intuitive or familiar coordinate pairs. The axial Lode coordinate σ_z is the hydrostatic component of the stress, and it is related to pressure p by $\sigma_z = \sqrt{3}p$. The Lode radius σ_r is a measure of shear stress, and it is related to the conventional measure of shear stress, $q = \sigma_A - \sigma_L$, by $\sigma_r = q\sqrt{2/3}$. Thus, not only may a plot of σ_r vs. σ_z be regarded as a "side view" of an isotropic yield surface, such a plot also may be seen as loosely depicting shear strength vs. pressure, with the only difference being constant scaling of the axes. The Lode coordinates represent decomposition of the tensor into isotropic and deviatoric parts, which reveals structure in simple idealized solid mechanics theories. For example, with the Lode measures for axisymmetric problems, the isotropic form of Hooke's Law becomes simply

$$\begin{bmatrix} \dot{\sigma}_z \\ \dot{\sigma}_r \end{bmatrix} = \begin{bmatrix} 3K & 0 \\ 0 & 2G \end{bmatrix} \begin{bmatrix} \dot{\epsilon}_z \\ \dot{\epsilon}_r \end{bmatrix} \tag{3.12}$$

where the 2×2 matrix is the elastic tangent stiffness tensor $\mathbb{C}$, K is the bulk modulus, and G is the shear modulus. Of course, the general form for incremental plasticity becomes

$$\begin{bmatrix} \dot{\sigma}_z \\ \dot{\sigma}_r \end{bmatrix} = \begin{bmatrix} T_{zz} & T_{zr} \\ T_{rz} & T_{rr} \end{bmatrix} \begin{bmatrix} \dot{\epsilon}_z \\ \dot{\epsilon}_r \end{bmatrix} \tag{3.13}$$

For simplicity, we may write this in a more compact notation as simply $\dot{\boldsymbol{\sigma}} = T\dot{\boldsymbol{\epsilon}}$, where it must be understood from context that $\dot{\boldsymbol{\sigma}}$ and $\dot{\boldsymbol{\epsilon}}$ are 2x1 vectors, while T is a 2x2 matrix.

Our analysis of laboratory data will *not* presume that a classical (incrementally linear) plastic tangent stiffness tensor even exists. Suppose that incremental nonlinearity

is observed in the data, but only incrementally linear plasticity models are available in a finite element code. Then a short-term workaround is needed while awaiting model enhancements. A rational strategy for interim use of existing classical plasticity models would set the incrementally linear parameters to values that minimize error with observed incrementally nonlinear data. In analogous problems involving scalars (instead of tensors), the rational approach is to use a least-squares fit to nonlinear data until a nonlinear model is available.

In our more general case, for which the data consist of a collection of stimulus vectors and their corresponding response vectors, an unweighted least-squares best linear fit to the data is obtained as follows: (1) place the stimulus vectors into columns of a matrix $[S]$; (2) place the corresponding response vectors into columns of a matrix $[R]$; and (3) evaluate the best-fit linear transformation matrix $[L] = [R][S]^{(-1)}$; where the superscript "(-1)" denotes the pseudo-inverse (also called the Moore-Penrose inverse, and is available in most numerical linear algebra packages, and required in data analysis because $[S]$ is generally nonsquare). The pseudoinverse is an ordinary inverse if there are exactly the same number of linearly independent stimulus vectors as the dimension of the space. The residual error of the approximation is quantified by the norm of $[R] - [L][S]$. Of course, a weighted linear regression may be used if greater accuracy for particular loading directions is desired. Incidentally, the experiments described in this report are all stress controlled. Therefore, the stimulus matrix $[S]$ holds the stress increment vectors, and the response matrix $[R]$ holds the measured strain increment vectors (interpolated to the current material state, as described in Section 3.4). Therefore, the $[L]$ matrix computed in our data analysis is actually the tangent compliance, $[L] = [T]^{-1}$.

As discussed above, this method allows a particular constitutive model to be fit to the experimental data, with a quantitative measure of the goodness of the fit. This is done using classical incrementally-bilinear plasticity theory. For this reason, the governing equations of classical plasticity theory will briefly be outlined here and then specialized to axisymmetric loading using the Lode coordinates discussed above.

In classical plasticity theory, the plastic tangent stiffness $\mathbb{T}$ is given by

$$\mathbb{T} = \mathbb{C} - \frac{1}{\mu}\boldsymbol{P} \otimes \boldsymbol{Q} \tag{3.14}$$

where $\boldsymbol{P} = \mathbb{C} : \hat{\boldsymbol{M}}$ (in which $\hat{\boldsymbol{M}}$ is the unit flow direction) and $\boldsymbol{Q} = \mathbb{C} : \hat{\boldsymbol{N}}$ (in which $\hat{\boldsymbol{N}}$ is the unit normal to the yield surface), and $\mu = \boldsymbol{P} : \hat{\boldsymbol{N}} + H$ (in which H is the "ensemble hardening modulus" [2]). For axisymmetric loading, the 81 component fourth-order plastic stiffness $\mathbb{T}$ reduces to the four-component matrix in Eq. (3.13). Specifically,

$$T = C - \frac{1}{\mu}P \otimes Q \tag{3.15}$$

where

$$\begin{bmatrix} P_z \\ P_r \end{bmatrix} = \begin{bmatrix} C_{zz} & C_{zr} \\ C_{rz} & C_{rr} \end{bmatrix} \begin{bmatrix} M_z \\ M_r \end{bmatrix} \tag{3.16}$$

$$\begin{bmatrix} Q_z \\ Q_r \end{bmatrix} = \begin{bmatrix} C_{zz} & C_{zr} \\ C_{rz} & C_{rr} \end{bmatrix} \begin{bmatrix} N_z \\ N_r \end{bmatrix} \tag{3.17}$$

$$\mu = P \cdot N + H \tag{3.18}$$

and the subscripts r and z indicate the components in the corresponding Lode coordinate directions. The four components of the elastic tangent stiffness C can be found from the four loading increments that are taken to be elastic increment directions. The validity of the assumption that these directions correspond to elastic unloading is confirmed by verifying that the measured plastic strain increments from these loading directions is small.

Knowing the plastic and elastic tangent stiffness tensors, as computed directly from the experimental data, will allow M and N to be calculated directly from the experimental data. To do this we solve Eq. (3.15) for the second term on the right, which we will label A:

$$A = C - T = \frac{1}{\mu}P \otimes Q \tag{3.19}$$

If classical plasticity theory applies, then, by properties of dyadic multiplication, the rows of A would be scalar multiples of Q and the columns would be scalar multiples of P. Otherwise, if classical plasticity is not strictly applicable (e.g., if the rows or columns of A are not multiples of each other), but if we nevertheless seek a best fit to classical plasticity, then a method is needed to assign values to P and Q. To find

the directions of P and Q we perform a polar decomposition of A. To perform this decomposition we define:

$$
\begin{aligned}
U^2 &= A^T \cdot A \\
&= (Q \otimes P) \cdot (P \otimes Q) \\
&= (P \cdot P) Q \otimes Q
\end{aligned}
\tag{3.20}
$$

As shown, U^2 will be a scalar multiple of the dyad $Q \otimes Q$. U^2 should then have one large eigenvalue and one small eigenvalue (identically zero if classical plasticity applies). The eigenvector associated with the large eigenvalue will be in the direction of Q. Similarly we define:

$$
\begin{aligned}
V^2 &= A \cdot A^T \\
&= (P \otimes Q) \cdot (Q \otimes P) \\
&= (Q \cdot Q) P \otimes P
\end{aligned}
\tag{3.21}
$$

Again, the eigenvector associated with the largest eigenvalue of V^2 will be in the direction of P. We now use the definitions of P and Q to write:

$$
P^* = \gamma C \cdot M
\tag{3.22}
$$

$$
Q^* = \beta C \cdot N
\tag{3.23}
$$

where γ and β are some unknown scalars, and P^* and Q^* are scalar multiples of P and Q respectively. Since $\mathbb{C}$ is known from the unloading vectors, Eqs. (3.16) and (3.17) may be solved for the directions of M and N:

$$
M^* = C^{-1} \cdot P^*
\tag{3.24}
$$

$$
N^* = C^{-1} \cdot Q^*
\tag{3.25}
$$

where $*$ is again used to indicate some scalar multiple of a variable, which may then be used to generate a unit vector in the direction of the vector.

3.6   Discussion of Results

3.6.1   Incremental Nonlinearity

Figures 3.4 and 3.5 show the strain response envelopes for three different tests. These envelopes are constructed from interpolated strain increments produced during the second and third loading cycles, respectively. The solid lines in these plots are a

representation of the best-fit elastic and plastic tangent stiffness tensors, which were found using the pseudo-inverse technique discussed in Section 3.5.

As described in Section 3.4, since each of these tests used a different level of confining stress, and began the incremental loading cycle at a different stress state, the response to a given loading cycle would not be expected to be the same for each test. For example, as Fig. 3.4 indicates, during loading cycle 2, the plastic strain increments of test 2 are much greater than those of test 1. This is because for test 2, cycle 2 occurs much closer to the failure point than does cycle 2 of test 1. The results from each cycle are merely plotted in the same figure for convenience.

The important aspect of the plots in Figs. 3.4 and 3.5 is the distribution of the plastic strain increments for each loading direction (each is labeled with an "x"). As the figures illustrate, to varying degrees, the direction of the plastic strain increments is observed to change with the loading direction. This dependence appears to be stronger for the material states where large plastic strains are observed. For example, in the results from test 1 shown in Fig. 3.4, the plastic strain increments, which are small relative to the other tests, all lie in nearly a straight line (with the exception of the one point in the third-quadrant, which is discussed below). In contrast, the plastic strain increment directions change significantly with the directions of the stress increments in Fig. 3.4 for test 2, which involved larger plastic strain increment magnitudes. This suggests an incrementally nonlinear response, which is not consistent with classical plasticity theory.

Another indication that these data tend to invalidate a classical regular flow rule is seen by examining the ellipses representing the plastic and elastic tangent stiffness tensors. The elastic tangent stiffness tensor is represented by the ellipse at the bottom of each strain envelope. In each case the elastic tangent stiffness tensor appears to accurately represent the strain increments for the anticipated elastic unloading directions. Even though these increments are anticipated to correspond to elastic unloading, to verify that the resulting deformation is elastic, the plastic strain increments for these directions were measured and are displayed in the plots. For all of these loading directions the measured plastic strain was small. This, together with the good fit of the elastic tangent stiffness ellipse to these increments, seems

to validate the original proposition that these are nearly perfectly elastic unloading directions.

In contrast to the good fit of the elastic tangent stiffness ellipse, the plastic tangent ellipse does not fit the data as well in all cases. The most important discrepancy is seen in the plots in Fig. 3.4, where the plastic strain increments are larger because each specimen is closer to failure. According to classical plasticity theory, the strain response envelope ought to be accurately described by two ellipses (one for each of the two tensorial zones). These two ellipses also ought to intersect. In other words, there should not be a discontinuity in the strain response envelope. This condition was not enforced with the least-squares fit to the data. Obviously, this requirement could be enforced, but this would result in a poorer fit to the total strain increments for the plastic loading directions. For example, consider the plot for test 2 in Fig. 3.4. If the ellipse corresponding to the plastic tangent stiffness were drawn such that it intersected the elastic tangent ellipse, then it clearly would be too narrow to pass through some of the strain increments for the plastic loading directions. In other words, the strain response envelope is wider at the top than at the middle, which is not compatible with the two-ellipse response envelope required by classical plasticity theory.

The plastic strain increments in the third quadrant for test 1 merit some discussion. The increments shown for Test 1 in Figs. 3.4 and 3.5 are not anomalies, but were observed for every load increment B in that test. This loading direction is of particular interest because it lies in or near the Sandler-Rubin wedge for models that use a pressure-dependent yield strength and a nonassociative flow rule. Some degree of pressure dependence in the yield strength was observed in these tests. This means that loading increment B should be directed outward from the yield surface, but at a relatively shallow angle. For such a stress increment, the corresponding plastic strain increment would be expected to be small compared to the total strain increment. Since the plastic strain increments are small for these loading increments, they are more prone to experimental error. Nevertheless, the fact that every loading increment B exhibited this behavior is enough to suggest that there may be something at odds with classical plasticity theory occurring for loads in this direction.

As discussed in Section 3.5, even if classical plasticity theory does not provide an optimal description of the experimental data, the data analysis technique presented in that section nevertheless provides a means for determining the best fit of classical parameters to the data. Using these best-fit tangent stiffness tensors, the directions of the yield surface normal N and plastic strain rate direction M were calculated using Eqs. (3.19) through (3.23). The results of these calculations are found in Table 3.2. The directions of M and N do not coincide for any of the cases, which seems to indicate that if only a classical plasticity model is available, a nonassociative flow rule provides a better fit than an associative flow rule.

3.7 Conclusion

Systematic laboratory experiments have been conducted to validate or invalidate assumptions common to virtually all plasticity models used in production-level engineering simulations. A particular goal has been to resolve the paradox that nonassociativity has been experimentally well established for most materials (including metals), while at the same time any form of nonassociativity admits the physically inadmissible Sandler-Rubin instability, which is equivalent to spontaneous motion from a quiescent state. Noting that the stress increments in standard testing are significantly different from the increments that induce the Sandler-Rubin instability, it was conjectured that a revision might be required in engineering plasticity models that allows the plastic tangent tensor to vary with the loading direction. Such a feature, if observed, would correspond to a need to revise existing plasticity theories to accommodate incremental nonlinearity. Testing for this possibility required nonstandard tests that aim to quantify the effect of a variety of loading directions on the material response.

For tractability, the laboratory experiments were limited to axisymmetric loading, and changes in the loading direction were achieved through independent control of axial and lateral components of stress. A new technique was developed to interpolate repeated pairs of stimulus-response vectors from a cyclic loading path (each occurring at a different material state) to a common material state.

A cyclic sequence of stress increments was applied to nonmonotonically move

the stress state through stress space. Additionally a means to interpolate repeated pairs of stimulus-response vectors to any desired point along the loading path was developed. The result of this data analysis is information about material response to stress increments in eight different directions. The response vectors were visualized using strain-response diagrams (Gudehus diagrams), which simply join the strain increment vectors at their tails so that the tips of these vectors form a closed curve. If the classical plasticity assumption of incremental linearity were correct, then the Gudehus diagram for total strain increments would be an ellipse in elastic loading and the continuous union of two ellipses in elastic-plastic loading. Furthermore, the plastic strain increments would all lie along a single line. The results of this study, however, suggest that as the specimen approaches failure, the plastic strain increment direction increasingly depends upon the direction of the applied stress increment. This is a manifestation of incremental nonlinearity, which, for example, could correspond to formation of vertices in the yield surface. This is further evidenced by the non-ellipsoidal shape of the strain response envelope for plastic loading directions.

Even though the data suggest an incrementally nonlinear response, there are currently few engineering plasticity models that include incremental nonlinearity. The new data analysis technique presented allows the classical plasticity parameters that best fit the data to be calculated. By performing these calculations, it was found that a classical nonassociative model fits the data better than a classical associative model. However, as discussed in Chapter 2, nonassociative models have been shown to produce nonphysical instabilities for certain loading directions. Therefore, pending much needed further experimental data for the effect of changes in the loading direction, it seems prudent to adopt nonclassical plasticity theories such as the extended flow rule (EFR) described in Chapter 2.

input (stimulus) vectors

output (response) vectors
for linear transformation

(a)

(b)

output (response) vectors
for nonlinear transformation

output (response) vectors
for nonlinear transformation

(c)

(d)
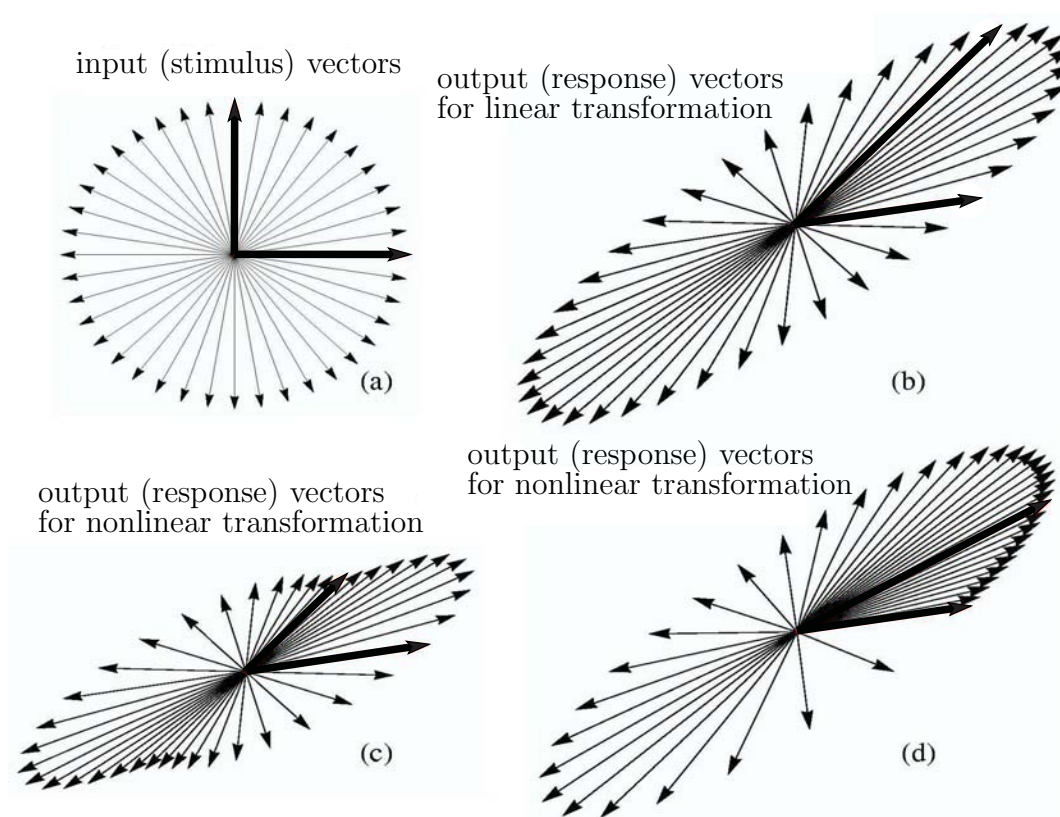
Figure 3.1. Visualization of vector transformations.
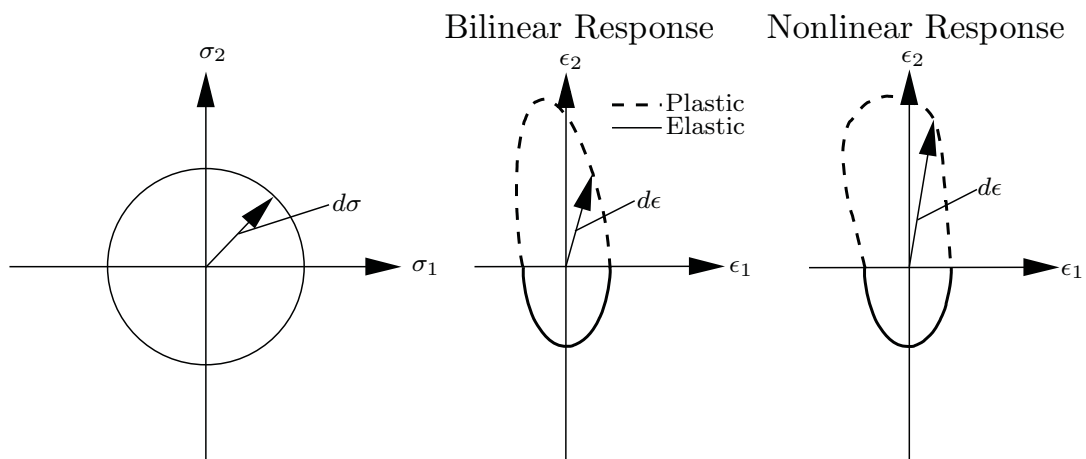
Figure 3.2. Sketch of Gudehus strain response diagrams for an incrementally bilinear and nonlinear response. The response to the stress increments that form a circle in stress space (left) is plotted in the corresponding strain space. An incrementally bilinear response (center) is characterized by two intersecting ellipses, each of which corresponds to a tensorial zone. An incrementally nonlinear response (right) is characterized by a more general envelope shape.
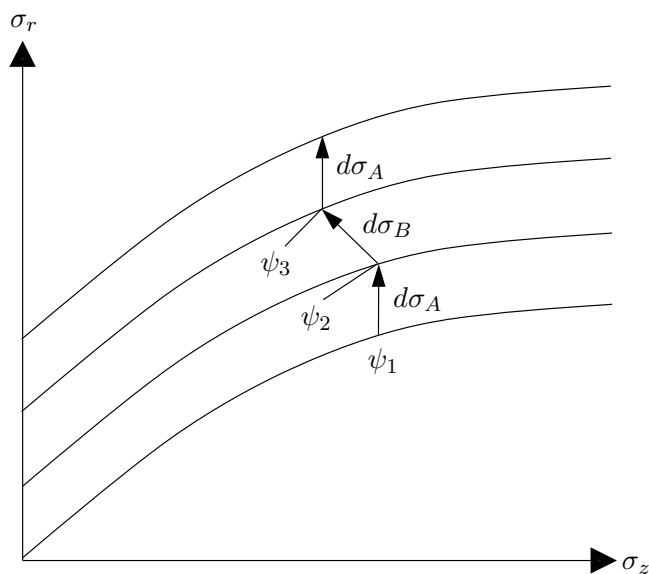
Figure 3.3. A simple cyclically applied incremental loading scheme. Beginning at material state ψ_1, a stress increment $d\sigma_A$ is applied, changing the material state to ψ_2. A stress increment $d\sigma_B$ is then applied, changing the material state to ψ_3. Finally, $d\sigma_A$ is applied beginning at material state ψ_3.
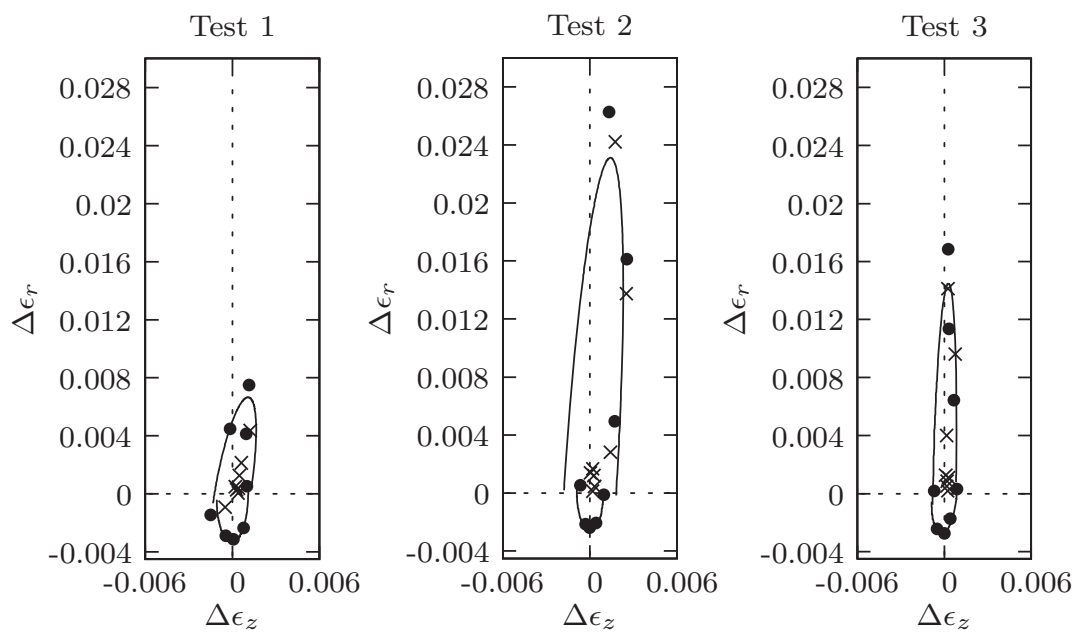
Figure 3.4. Response envelopes for the second stress cycle of tests 1, 2 and 3. Dots indicate total strain increments, "x" indicates a plastic strain increment.
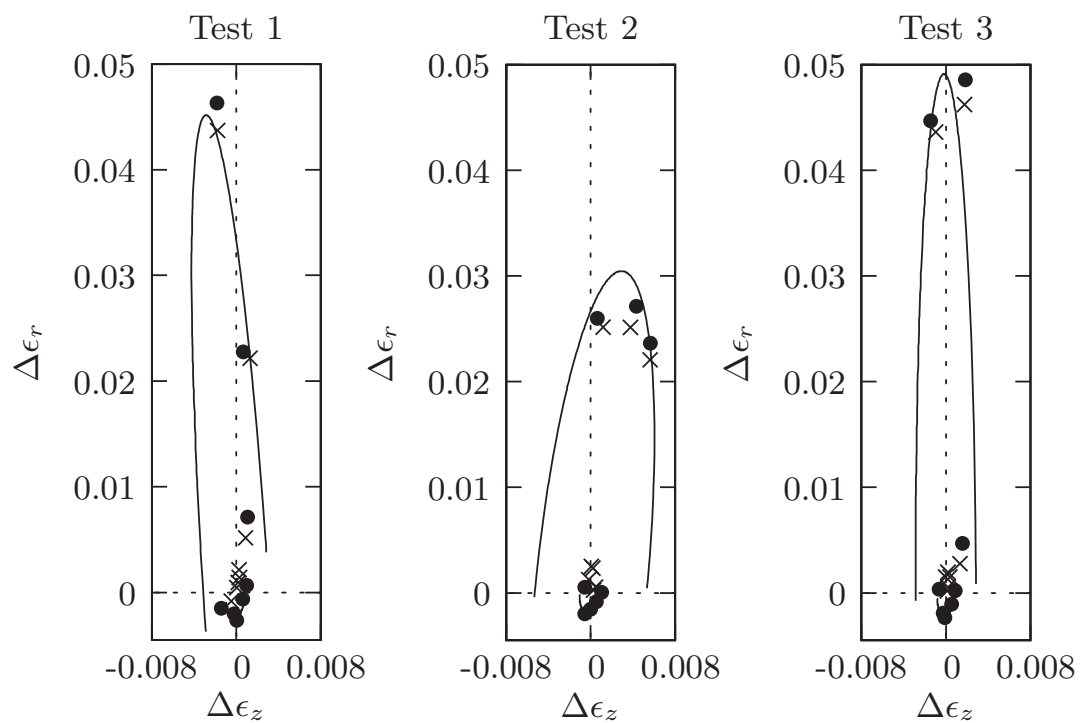
Figure 3.5. Response envelopes for the third stress cycle of tests 1, 2, and 3. Dots indicate total strain increments, "x" indicates a plastic strain increment.

Table 3.1. Description of stress increments where ϕ is the angle formed with the hydrostatic compression axis, and $\dot{\Sigma}$ is the total increment magnitude.

Leg	ϕ	$\dot{\Sigma}$
A	90°	300 psi
B	180°	300 psi
C	35°	300 psi
D	125°	300 psi

Table 3.2. Direction of the yield surface normal $\hat{N}$ and the plastic strain rate $\hat{M}$ referenced to the hydrostatic compression axis.

(a) Test 1

Step	θ_M	θ_N
2	39°	66°
3	105°	146°
4	125°	198°

(b) Test 2

Step	θ_M	θ_N
2	99°	120°
3	153°	173°
4	-	-

(c) Test 3

Step	θ_M	θ_N
2	83°	122°
3	116°	163°
4	131°	179°

CHAPTER 4

A NONLOCAL PLASTICITY MPM
FORMULATION

4.1   Abstract

A new multivariate fixed-point iteration scheme is devised for solving the coupled dynamic integral equations governing nonlocal plasticity using the Material Point Method (MPM). Novel use of the MPM grid for particle-particle communications results in a simple and efficient, matrix-free method. Moreover, a straightforward method for deriving a convergence criterion for this method is developed and applied to a classical verification problem that is well known to be mesh dependent with a local model, but is shown to be mesh independent with the new nonlocal MPM formulation.

4.2   Introduction

The material point method (MPM) is a particle-based method for solving large-deformation solid mechanics problems [40, 41]. In this method, the problem domain is discretized into particles that carry material data such as mass, velocity, internal state variables, etc. At each time step, the mass, velocity, and internal force are projected from the particles to a "background" grid, which is typically (though not necessarily) taken to be Eulerian. The equations of motion are solved on the background grid, and the updated velocity and acceleration fields at the grid nodes are then mapped to the particles to update the particle position and velocity, respectively. The updated grid velocity field is used to calculate the velocity gradient, rate of deformation, and updated deformation gradient tensors at each particle, which then may be used by the constitutive model to update the stress at each particle. The MPM equations

and algorithm are summarized in Section 4.3. For a more complete description of the method see Steffen and Wallstedt for a review [61]. An implicit version of the MPM has also been developed [62, 63], but only the explicit MPM is considered in this paper.

The material point method has successfully been used to solve a wide variety of solid mechanics problems including fluid-structure interaction [64], finite-deformation plasticity [65], fracture mechanics [66, 67], and impact/penetration [68, 69]. Many potential areas of application of the MPM involve material softening (i.e., loss of strength due to inelastic deformation). When softening occurs, plastic deformation often localizes into a discrete region, which has been shown to result in a loss of hyperbolicity and ill-posedness of the governing equations [70, 30]. The consequence of this ill-posedness, in numerical simulations, is that the localization zone becomes proportional to the mesh spacing. As the mesh is refined, the localization zone therefore becomes ever smaller, and the failure energy of the structure approaches zero. In a real material, the size of a localization zone would be determined by the length scale of the underlying material microstructure (grain size, void distribution, etc.). However, local material models possess no intrinsic length scale from which the size of a localization zone can be established.

Nonlocal plasticity theory has been developed to introduce an intrinsic length scale to plasticity models. This intrinsic length scale results in two important characteristics. First it serves as a localization limiter, which restores the well-posedness of the initial boundary-value problem by limiting the width of a localization zone [71, 72, 73]. Second, it results in the prediction of a size effect, which causes the length scale of a structure relative to the material's structure to influence its mechanical response, as has been observed in the laboratory [74, 75]. This is in contrast to a traditional local continuum material where no intrinsic length scale is associative with the material, and hence, no size effect is predicted.

Here the term nonlocal is used to describe any type of plasticity model that includes an intrinsic length scale. Two classes of nonlocal models have emerged in the literature: strongly nonlocal and weakly nonlocal. The strongly nonlocal formulations include nonlocal models of the integral type, as well as the implicit gradient model of

Engelen and Geers [76, 77]. The weakly nonlocal models include the explicit gradient models [73, 78]. For a comparison of the explicit gradient, implicit gradient, and integral-type nonlocal models see the paper by Peerlings et al. [79]. For a more complete survey of the various nonlocal models that have been developed see the papers by Bazant [80] and Di Luzio and Bazant [50].

In terms of implementation, a local plasticity model results in an uncoupled set of algebraic constitutive equations, whereas nonlocal formulations, when discretized, result in a coupled set of constitutive equations. The integral-type formulation results in a coupled set of integral equations [72, 51]. The explicit gradient formulation results in a partial differential equation which must be solved over the plastic portion of the domain [78]. The implicit gradient formulation results in a partial differential equation of the Helmholtz type which must be solved simultaneously with the equations of motion or equilibrium [76]. Various methods have been employed to solve these additional equations. The focus of this paper is solving the equation of the integral-type nonlocal models.

The integral-type nonlocal models have a few distinct advantages and disadvantages as compared to the gradient models. Both the integral-type and implicit gradient models are strongly nonlocal, which makes them effective at limiting the size of localized regions and thereby restoring the well-posedness to localization problems. An advantage of nonlocal models is that no additional boundary conditions are necessary for the plastic strain field, as is the case with both implicit and explicit gradient models. The primary disadvantage to the integral-type models is the difficulty of solving the resulting system of integral equations. The purpose of this paper is to present a new method of solving this coupled system of integral equations using the material point method (MPM). The approach taken in this paper is closely related to that used by Stromberg and Ristinmaa with the FEM, however there are several primary unique contributions made by the present work.

Firstly, whereas integral-type nonlocal models have been implemented previously using other methods [72, 51, 81, 82, 83], this is the first paper to present a nonlocal plasticity algorithm for the MPM.

Secondly, a method for evaluating the nonlocal integrals is presented that uses

the MPM background grid rather than body-fixed Lagrangian points. This scheme eliminates the need to maintain a list of "neighboring" material points within the support domain of the nonlocal weighting function around each material point. This is particularly important for large deformation problems where the number and identity of the particles within the nonlocal support domain of a particle changes in time.

The third unique contribution made by the present work is a straightforward method for deriving a convergence criterion for the new method is presented. Stromberg and Ristinmaa demonstrated that their iteration scheme converged for the problems considered in that work, but they did not derive a general convergence criterion. In the present work, we show that a similar iteration scheme may be derived using a multivariate fixed-point iteration scheme. Using a Drucker-Prager yield model, Section 4.5 summarizes various fixed-point systems that can be derived from the same set the yield equations. The Banach contraction mapping theorem is used to derive a general convergence criterion for two of these possible iteration schemes for the Drucker-Prager model. The resulting convergence criteria reveal under what conditions each fixed-point formulation is preferred.

The organization of the paper is as follows. Section 4.3 is a brief overview of the MPM. Section 4.4 provides an overview of the equations of nonlocal plasticity. In Section 4.5 we derive two fixed-point iteration schemes for a nonlocal Drucker-Prager plasticity model. Section 4.6 discusses the implementation of the fixed-point iteration scheme within the MPM. Finally, in Section 4.7, results are presented from a simple localization problem. The nonlocal plasticity method presented here is shown to cause the localization zone to converge to a finite width as the mesh is refined. The width of the localization region is shown to be proportional to the nonlocal length scale parameter. Additionally, the behavior of a structure is shown to depend upon the ratio of the specimen length scale and the nonlocal length scale.

4.3   Review of the Material Point Method

With the material point method (MPM), the problem domain is discretized into a set of Lagrangian material point particles. Each MPM particle represents a finite Lagrangian volume of the material, and is used to track the properties of that volume

(e.g., mass m_p, volume V_p, density $\rho_p = m_p/V_p$, stress $\boldsymbol{\sigma}_p$, deformation gradient tensor $\boldsymbol{F}_p$, internal variables, etc.). The method also makes use of a "background" grid. Though it is not required by the method, a uniform, structured Eulerian background grid is often used. For each time step, the equations of motion are solved on the background grid in the same manner as with the finite element method (FEM). Accordingly, the lumped mass array is given by

$$m_i = \int_\Omega \rho(\boldsymbol{x}) S_i(\boldsymbol{x}) dV \tag{4.1}$$

where ρ is the mass density, and S_i is the shape function associative with the ith grid node. With the FEM, the integral in Eq. (4.1) is broken up, without loss, into a sum of integrals over element domains. With the MPM, on the other hand, the integral in Eq. (4.1) is broken up into a sum of integrals over nonoverlapping particle domains Ω_p:

$$m_i = \sum_p \rho_p \int_{\Omega_p} S_i(\boldsymbol{x}) dV \tag{4.2}$$

where ρ_p is the density of the pth particle, which is assumed to be constant over the particle domain. Similarly, the internal force array is

$$\boldsymbol{f}_i^{\text{int}} = -\sum_p \boldsymbol{\sigma}_p \cdot \int_{\Omega_p} \nabla S_i(\boldsymbol{x}) dV \tag{4.3}$$

In principle, each integral over the particle domain may be evaluated exactly if Ω_p is treated as the Voronoi cell for the particle. To avoid the need for finding the Voronoi tessellation, these integrals may be approximated as follows:

$$m_i = \sum_p m_p \phi_{ip} \tag{4.4}$$

and

$$\boldsymbol{f}_i^{\text{int}} = \sum_p \boldsymbol{\sigma}_p \cdot G_{ip} \tag{4.5}$$

where

$$\phi_{ip} = \frac{1}{V_p^*} \int_{\Omega^*} S_i^*(\boldsymbol{x}) \chi_p(\boldsymbol{x}) dV \tag{4.6}$$

$$\boldsymbol{G}_{ip} = \frac{1}{V_p^*} \int_{\Omega^*} \nabla S_i^*(\boldsymbol{x}) \chi_p(\boldsymbol{x}) dV \tag{4.7}$$

and

$$V_p^* = \int_{\Omega^*} \chi_p(\boldsymbol{x}) dV \tag{4.8}$$

Equations (4.6) and (4.7) have introduced a generalized integration domain Ω^*, as well as a weight function $\chi_p(\boldsymbol{x})$, and possibly an approximate shape function to allow these integrals to reduce to the various MPM formulations in the literature. If $S_i^*(\boldsymbol{x}) = S_i(\boldsymbol{x})$, $\Omega^* = \Omega_p$, and χ_p is the Dirac delta function, then the result is the standard MPM formulation [40]. If $S_i^*(\boldsymbol{x}) = S_i(\boldsymbol{x})$, $\Omega^* = \Omega_u$, with $\chi_p = 1$ on Ω_u and 0 elsewhere, where Ω_u is an undeforming cuboid, then the result is the "uGIMP" formulation [41]. Finally, if $S_i^*(\boldsymbol{x}) = S_i^{\mathrm{app}}(\boldsymbol{x})$, where $S_i^{\mathrm{app}}(\boldsymbol{x})$ is a linear interpolating function across the generalized domain $\Omega^* = \Omega_{\mathrm{CPDI}}$, and $\chi_p = 1$ on Ω_{CPDI} and 0 elsewhere, where Ω_{CPDI} is a parallelepiped that deforms with the particle's deformation gradient, then the result is the CPDI formulation [84].

Regardless of the MPM formulation that is used, the internal force vector, along with any external force vector f_i^{ext}, and the lumped mass m_i are used to solve for the nodal acceleration vector:

$$\boldsymbol{a}_i = \frac{\boldsymbol{f}_i^{\mathrm{int}} + \boldsymbol{f}_i^{\mathrm{ext}}}{m_i} \tag{4.9}$$

The updated grid velocities $\boldsymbol{v}_i$, are found using an explicit forward-Euler time integration scheme:

$$\boldsymbol{v}_i^{n+1} = \boldsymbol{v}_i^n + \boldsymbol{a}_i \Delta t \tag{4.10}$$

The velocity gradient at each particle is calculated using:

$$\nabla \boldsymbol{v}_p^{n+1} = \sum_i \boldsymbol{G}_{ip} \boldsymbol{v}_i^{n+1} \tag{4.11}$$

The symmetric part of the velocity gradient tensor is then used to update the stress state of each particle. Finally, the particle position, velocity are updated according to:

$$\boldsymbol{x}_p = \boldsymbol{x}_p^n + \sum_i \phi_{ip} \boldsymbol{v}_i \Delta t \tag{4.12}$$

and

$$\boldsymbol{v}_p = \boldsymbol{v}_p^n + \sum_i \phi_{ip} \boldsymbol{a}_i \Delta t \tag{4.13}$$

respectively.

As mentioned, all problem data (density, stress, etc.) are saved at particles. Accordingly, the continuous approximation to any field $h(\boldsymbol{x})$ is then described on the background grid as

$$h(\boldsymbol{x}) = \sum_i h_i S_i(\boldsymbol{x}) \tag{4.14}$$

where h_i is the nodal value on the grid, calculated from particle values, h_p, by

$$h_i = \frac{1}{m_i} \sum_p \phi_{ip} h_p m_p \tag{4.15}$$

The MPM formally belongs to the class of meshless methods for which fields are described by

$$h(\boldsymbol{x}) = \sum_p h_p B_p(\boldsymbol{x}) \tag{4.16}$$

in which $B_p(\boldsymbol{x})$ are particle basis functions. The computational advantage of the MPM is that these particle basis functions do not need to be constructed explicitly. In particular, substituting Eq. (4.15) into (4.14) shows that the MPM particle basis functions are

$$B_p(\boldsymbol{x}) = \sum_i \frac{m_p}{m_i} \phi_{ip} S_i(\boldsymbol{x}) \tag{4.17}$$

4.4 Nonlocal Plasticity

In nonlocal plasticity theory, as in classical elastoplasticity theory, the strain rate $\dot{\boldsymbol{\epsilon}}$ is assumed to be additively decomposed into elastic and plastic parts, $\dot{\boldsymbol{\epsilon}}^e$ and $\dot{\boldsymbol{\epsilon}}^p$, respectively:

$$\dot{\boldsymbol{\epsilon}} = \dot{\boldsymbol{\epsilon}}^e + \dot{\boldsymbol{\epsilon}}^p \tag{4.18}$$

The stress rate tensor $\dot{\boldsymbol{\sigma}}$ is given by elasticity theory according to

$$\dot{\boldsymbol{\sigma}} = \mathbb{C} \colon \dot{\boldsymbol{\epsilon}}^e \tag{4.19}$$

where $\mathbb{C}$ is the fourth-order elastic tangent stiffness tensor. The plastic strain rate is described by the flow rule according to Eq. (4.20):

$$\dot{\boldsymbol{\epsilon}}^p = \dot{\lambda} \hat{\boldsymbol{M}} \tag{4.20}$$

where $\dot{\lambda}$ is the "rate-like" plastic multiplier and $\hat{\boldsymbol{M}}$ is a unit tensor defining the direction of the plastic strain rate tensor.

Bazant and Lin's nonlocal plasticity model included a nonlocal average of the plastic strain rate tensor in the strain rate decomposition equation [72]. In that seminal work, every occurrence of the plastic strain rate tensor in classical theory was replaced with a nonlocal average. Subsequent work demonstrated that this is not necessary (and, in some cases, not sufficient) to regularize the governing equations [51, 50]. Specifically, nonlocal terms are needed only in the evolution equations for the internal state variables that drive softening.

As in classical plasticity, the yield function f is a scalar function of the stress tensor and a set of internal state variables that change in response plastic loading. Each internal state variable may either be a local or nonlocal variable. For simplicity, only one local internal state variable, η, and one nonlocal internal state variable, ζ, will be considered. Extension of the theory to account for any number of local or nonlocal internal state variables should be self evident.

The standard Kuhn-Tucker plastic consistency conditions are:

$$f\dot\lambda = 0, \quad f \leq 0, \quad \dot\lambda \geq 0 \tag{4.21}$$

These equations may equivalently be cast as a complementarity problem (c.f. [51]):

$$f = w, \quad w\dot\lambda = 0, \quad w \leq 0, \quad f \leq 0, \quad \dot\lambda \geq 0 \tag{4.22}$$

The solution to the complementarity problem consists of finding w and $\dot\lambda$, at least one of which must be zero, at each material point. In practical terms, this involves determining which particles are undergoing plastic deformation in a given time step, and determining the value of $\dot\lambda$ during that step. If $w \neq 0$, the actual value of w is not of interest.

Although within the plasticity community the complementarity form is an uncommon way of expressing the plastic consistency condition, this form highlights the fact that determining which particles are undergoing plastic deformation is an important part of the solution procedure. For a local model this involves only checking the sign of the yield function. As will be shown, for a nonlocal model, making this determination is not so trivial. The complementarity form of the consistency equation also results in a more straightforward means of expressing the iteration scheme described in the next section.

The local internal state variable η evolves according to

$$\dot{\eta} = h_\eta \dot{\lambda} \tag{4.23}$$

where h_η is the local hardening/softening modulus. The nonlocal internal state variable ζ evolves according to

$$\dot{\zeta} = h_\zeta \langle \dot{\lambda} \rangle \tag{4.24}$$

where h_ζ is the nonlocal hardening/softening modulus, and $\langle : \rangle$ is the nonlocal averaging operator defined by a weighted average integral over the entire problem domain Ω:

$$\langle \dot{\lambda} \rangle = \frac{1}{V_\alpha} \int_\Omega \alpha(\boldsymbol{x} - \boldsymbol{s}) \dot{\lambda}(\boldsymbol{s}) d\boldsymbol{s} \tag{4.25}$$

Here, $\boldsymbol{x}$ is the location of a given particle and $\alpha(\boldsymbol{x})$ is the nonlocal weighting function, and

$$V_\alpha = \int_\Omega \alpha(\boldsymbol{x} - \boldsymbol{s}) d\boldsymbol{s} \tag{4.26}$$

The divisor V_α normalizes the nonlocal average, and also serves an important role at boundaries. The weighting function of a particle that is adjacent to a material boundary will have a portion of its support outside of Ω. This portion of the weighting function will not contribute to V_α, thus reducing the value of V_α compared to that of an interior particle. The result is that the material near a boundary has a higher weighting in the nonlocal average than material far from a boundary. Unlike gradient plasticity models, no additional boundary conditions for the field of plastic multipliers is necessary.

A Gaussian bell curve is used for the nonlocal weighting function:

$$\alpha(\boldsymbol{x}) = \mathrm{Exp}\left[(-k \, \|\boldsymbol{x}\| \, / L)^2 \right] \tag{4.27}$$

where $k = (6\sqrt{\pi})^{\frac{1}{3}}$, and L is the nonlocal length scale. This choice for the nonlocal weighting function is not unique. The critical properties of the weighting function are the extent of the function's support, and the smoothness. It has been reported in the literature that a smooth weighting function results in a higher rate of convergence [72].

The generalized nonlocal model described here allows for both local and nonlocal hardening/softening. If h_η were zero, the result would be a purely nonlocal model, and if h_ζ were zero, a purely local model is recovered. Several studies in the literature advocate using both local and nonlocal terms [51, 85, 50]. Stromberg and Ristinmaa's model of this type, which was called an overlocal model by Di Luzio and Bazant, is obtained by letting $h_\eta > 0$ and $h_\zeta < 0$. If each internal variable is defined such that an increase in the internal variable tends to increase the yield strength, then an overlocal model corresponds to local contributions to hardening and nonlocal contributions to softening.

If a backward Euler implicit integration scheme is used for updating $\boldsymbol{\sigma}$, η, and ζ, the first equation in (4.22) may be written at the end of time step k as

$$f\left(\boldsymbol{\sigma}^n + \dot{\boldsymbol{\sigma}}^{n+1}\Delta t, \eta^n + h_\eta \dot{\lambda}^{n+1}\Delta t, \zeta^n + h_\zeta \langle\dot{\lambda}\rangle^{n+1}\Delta t\right) = w^{n+1} \qquad (4.28)$$

where the superscripted n refers to the time step number. In general the hardening moduli can change during plastic loading increments, but are often simply taken to be constant over a time step. Equations (4.18), (4.19) and (4.20) can be combined to give:

$$\dot{\boldsymbol{\sigma}} = \mathbb{C}{:}\dot{\boldsymbol{\epsilon}} - \dot{\lambda}\boldsymbol{A} \qquad (4.29)$$

where $\boldsymbol{A} = \mathbb{C}{:}\hat{\boldsymbol{M}}$. Substituting Eq. (4.29) into Eq. (4.28) gives

$$f(\boldsymbol{\sigma}_{\text{trial}} - \Delta\lambda\boldsymbol{A}, \eta^{n+1}, \zeta^{n+1}) = w^{n+1} \qquad (4.30)$$

where

$$\eta^{n+1} = \eta^n + h_\eta \dot{\lambda}^{n+1}\Delta t \qquad (4.31)$$

$$\zeta^{n+1} = \zeta^n + h_\zeta \langle\dot{\lambda}\rangle^{n+1}\Delta t \qquad (4.32)$$

and

$$\boldsymbol{\sigma}_{\text{trial}} = \boldsymbol{\sigma}^n + \mathbb{C}{:}\dot{\boldsymbol{\epsilon}}^{n+1}\Delta t \qquad (4.33)$$

The objective of the nonlocal plasticity algorithm is to find the fields $\dot{\lambda}^{n+1}$, and w^{n+1}, that satisfy Eq. (4.30), ensuring that the plastic consistency condition is satisfied at each time step.

4.5 Fixed-Point Iteration Scheme for Linear Drucker-Prager Yield Function

For simplicity, we restrict the discussion to a linear Drucker-Prager yield function with linear isotropic hardening/softening. The discretization method used here may nevertheless be used for any yield function desired. The Drucker-Prager yield function is:

$$f(\boldsymbol{\sigma}, \eta, \zeta) = \sqrt{J_2} + \beta I_1 - k_o - \eta - \zeta \tag{4.34}$$

where $J_2 = \frac{1}{2}\boldsymbol{S}{:}\boldsymbol{S}$, $\boldsymbol{S}$ is the deviatoric stress tensor, and $I_1 = \mathrm{Tr}(\boldsymbol{\sigma})$. The material parameters are β, and k_o. These parameters are proportional to the friction angle and cohesion, respectively. The direction of the plastic strain rate tensor is prescribed to be proportional to the unit normal to the plastic flow potential surface. The plastic flow potential is taken to have the same functional form as the yield function. The only material parameter affecting the direction of the plastic strain rate tensor is the dilatation parameter β_p. The dilatation angle controls the ratio of volumetric to deviatoric plastic strain. If β_p is chosen to coincide with β, then the plastic potential and the yield surface are identical, which is called an associative model. The plastic flow direction is then

$$\hat{\boldsymbol{M}} = \frac{\frac{1}{\sqrt{2}}\frac{\boldsymbol{S}^{n+1}}{\|\boldsymbol{S}^{n+1}\|} + \beta_p\boldsymbol{I}}{\sqrt{\frac{1}{2} + 3\beta_p^2}} \tag{4.35}$$

where, consistent with the backward-Euler scheme, $\boldsymbol{S}^{n+1}$ is the deviatoric stress tensor at the end of the time step, and $\boldsymbol{I}$ is the second-order identity tensor. Using the yield function in (4.34), and substituting these expressions into equation (4.30) for plastic particles ($w = 0$) under the addition assumption that the elastic stiffness is constant and isotropic, the yield function at the end of the step evaluates to

$$f(\boldsymbol{\sigma}_{\mathrm{trial}} - \Delta\lambda\boldsymbol{A}, \eta^{n+1}, \zeta^{n+1}) = f_{\mathrm{trial}} - \Delta\lambda\frac{G}{\sqrt{\frac{1}{2} + 3\beta_p^2}} - \Delta\lambda\frac{9\beta K\beta_p}{\sqrt{\frac{1}{2} + 3\beta_p^2}}$$
$$- h_\eta\Delta\lambda - h_\zeta\langle\Delta\lambda\rangle = 0 \tag{4.36}$$

where G is the shear modulus, K is the bulk modulus, $\Delta\lambda = \dot{\lambda}\Delta t$, and

$$f_{\mathrm{trial}} = f(\boldsymbol{\sigma}_{\mathrm{trial}}, \eta^n, \zeta^n) \tag{4.37}$$

Since $\langle \Delta\lambda \rangle$ is an integral operator that includes contributions from other particles, Eq. (4.36) gives a coupled system of integral equations to be satisfied at each plastic particle. The new technique presented in this paper solves this system by first transforming it into an equivalent system of fixed-point equations. There are several ways of transforming Eq. (4.36) into a system of fixed-point equations, some resulting in better convergence behavior than others. In most cases, convergence depends upon the selected material parameters. To illustrate this point, two fixed-point expressions of Eq. (4.36) are examined. The first is generated by taking all local values of $\Delta\lambda$ to be the updated value, with the nonlocal term being evaluated using the previous estimate for $\Delta\lambda$. This gives

$$f_{\text{trial}} - \Delta\lambda^{k+1} \frac{G}{\sqrt{\frac{1}{2} + 3\beta_p^2}} - \Delta\lambda^{k+1} \frac{9\beta K \beta_p}{\sqrt{\frac{1}{2} + 3\beta_p^2}}$$
$$- h_\eta \Delta\lambda^{k+1} - h_\zeta \langle \Delta\lambda^k \rangle = 0, \quad (4.38)$$

where k is the iteration number. Solving this expression for $\Delta\lambda^{k+1}$ gives

$$\Delta\lambda^{k+1} = \frac{f_{\text{trial}} - h_\zeta \langle \Delta\lambda^k \rangle}{\frac{G}{\sqrt{\frac{1}{2}+3\beta_p^2}} + \frac{9\beta K \beta_p}{\sqrt{\frac{1}{2}+3\beta_p^2}} + h_\eta} \quad (4.39)$$

The other fixed-point equation considered is the same as that in Eq. (4.39) except that the local hardening term (i.e., coefficient of h_η) is evaluated using the previous estimate for $\Delta\lambda$:

$$f_{\text{trial}} - \Delta\lambda^{k+1} \frac{G}{\sqrt{\frac{1}{2} + 3\beta_p^2}} - \Delta\lambda^{k+1} \frac{9\beta K \beta_p}{\sqrt{\frac{1}{2} + 3\beta_p^2}}$$
$$- h_\eta \Delta\lambda^k - h_\zeta \langle \Delta\lambda^k \rangle = 0. \quad (4.40)$$

The resulting fixed-point equation is

$$\Delta\lambda^{k+1} = \frac{f_{\text{trial}} - h_\eta \Delta\lambda^k - h_\zeta \langle \Delta\lambda^k \rangle}{\frac{G}{\sqrt{\frac{1}{2}+3\beta_p^2}} + \frac{\beta 9 K \beta_p}{\sqrt{\frac{1}{2}+3\beta_p^2}}} \quad (4.41)$$

The convergence criterion for each of these fixed-point schemes is found by computing the derivative of $\Delta\lambda^{k+1}$ with respect to $\Delta\lambda^k$. Applying the Banach fixed-point theorem, this fixed-point scheme will converge to a unique fixed-point if

$$\mathscr{L} = N_\alpha \left\| \frac{\partial \Delta\lambda^{k+1}}{\partial \Delta\lambda^k} \right\| < 1 \quad (4.42)$$

where N_α is the number of particles within the support of $\alpha(\boldsymbol{x})$. $\mathscr{L}$ is called the Lipschitz constant of the system of equations. The Lipschitz constant for the first iteration scheme is bounded by

$$\mathscr{L}_1 \leq N_\alpha \left\| \frac{h_\zeta}{\frac{G}{\sqrt{\frac{1}{2}+3\beta_p^2}} + \frac{9\beta K \beta_p}{\sqrt{\frac{1}{2}+3\beta_p^2}} + h_\eta} \right\| \tag{4.43}$$

where, referring to Eq. (4.25), use has been made of the fact that

$$\frac{\partial \langle \Delta\lambda^k \rangle}{\partial \Delta\lambda^k} \leq 1 \tag{4.44}$$

Similarly the Lipschitz constant for the second fixed-point scheme is bounded by:

$$\mathscr{L}_2 \leq N_\alpha \left\| \frac{h_\eta + h_\zeta}{\frac{G}{\sqrt{\frac{1}{2}+3\beta_p^2}} + \frac{9\beta K \beta_p}{\sqrt{\frac{1}{2}+3\beta_p^2}}} \right\| \tag{4.45}$$

Smaller values of the Lipschitz constant correspond to faster convergence to the fixed point. Notice that for the local case ($h_\zeta = 0$) the Lipschitz constant for the first scheme is zero, indicating that the scheme will converge to the exact solution in one step. This is to be expected since purely local linear hardening/softening corresponds to a single uncoupled linear equation. For a nonlocal or overlocal model, the rate of convergence depends upon the material parameters (h_η, h_ζ, G, K, β and β_p), as well as the number of particles within the support of the nonlocal weighting function (N_α). With the MPM it is generally a good practice to keep the number of particles per cell constant as the mesh is refined [86]. However, this practice leads to an increase in N_α as the mesh is refined, resulting in a reduction in the convergence rate. Of course, if the Lipschitz constant becomes greater than unity, the fixed-point scheme may diverge. Therefore, for materials for which the softening modulus is large enough to produce a Lipschitz constant greater than one, this fixed-point iteration scheme may not be suitable. However, as will be demonstrated with a case study problem in Section 4.7.2, the structural response may become brittle as a result of either a large softening modulus, or as a result of the structure's length scale being much larger than the length scale of the material's microstructure. Thus a structure may behave in a very brittle manner without necessarily requiring large softening modulus.

For nonlinear hardening/softening it would not generally be possible to algebraically transform the yield condition into a fixed-point system. While not demonstrated here, the same general procedure may nevertheless be used, but instead of algebraically solving the yield equation for $\Delta\lambda^{k+1}$, a Newton iteration scheme can be used to generate a fixed-point equation. Stromberg and Ristinmaa's algorithm [51] is a special case of this method. In this case a convergence criterion can be derived in the same way as when the fixed-point equations are algebraically derived. Such a scheme is a nonlinear generalization of the Gauss-Seidel method. A detailed discussion of such schemes can be found in a text by Ortega [87].

4.6 Solution Strategy for the MPM

This section describes how the fixed-point iteration scheme presented in the previous section may be incorporated into the MPM. As mentioned in Section 4.2, the MPM saves field data at particles, and projects the data to grid nodes for solving field equations.

Referring to Eqs. (4.14) and (4.15), the standard MPM solution procedure uses particle values of a field, h_p, to construct a grid-based representation of that field, $h(\boldsymbol{x})$. The new nonlocal algorithm presented in this paper is distinguished from other nonlocal solvers in the literature by its use of this MPM mapping to evaluate the nonlocal integrals in the yield equations. As discussed below, this technique makes it unnecessary to build and maintain a list of which particles are involved in the nonlocal average of each particle. An outline of the algorithm is shown in Algorithm 1, and each step is described in detail below.

The first step in the nonlocal algorithm is to generate an initial estimate for which particles are undergoing plastic deformation, and an initial estimate for $\Delta\lambda$ at those particles. As is done with traditional local constitutive models, the trial stress is computed using the symmetric part of the velocity gradient, which is given in Eq. (4.11). If evaluating the yield function with the trial stress results in a negative value of the yield function, the particle is *tentatively* considered to be an elastic particle (i.e., $\dot{\lambda} = 0$; $w \neq 0$). If the trial stress state results in a zero or positive value for the yield function, then the particle is considered to be plastic (i.e., $\dot{\lambda} > 0$; $w = 0$).

An initial estimate for the increment of the plastic multiplier is found by neglecting nonlocal effects and using a backward Euler integration scheme [88]. Using Eq. (4.15), the estimate for the plastic multiplier increment is then projected to the grid nodes as

$$\Delta\lambda_i = \frac{1}{m_i}\sum_p \phi_{ip}\Delta\lambda_p m_p \tag{4.46}$$

Once the initial estimate for the plastic multiplier increment has been projected to the grid nodes, the initialization for the iterative scheme is complete.

Step two of the nonlocal algorithm is the main iteration loop. For each iteration, the nonlocal integral is evaluated for each plastic particle. This is done by first identifying which grid nodes are within the support domain of the nonlocal weighting function $\alpha(\boldsymbol{x})$. Then, the incremental form of the nonlocal integral in Eq. (4.25) is approximated by a discrete sum using

$$\langle\Delta\lambda\rangle_p = \frac{1}{M_\alpha}\sum_i \alpha(\boldsymbol{x}_p - \boldsymbol{x}_i)\Delta\lambda_i m_i \tag{4.47}$$

and

$$M_\alpha = \sum_{i=0}^{N_\alpha} \alpha(\boldsymbol{x}_p - \boldsymbol{x}_i)m_i \tag{4.48}$$

By using the nodal mass m_i in the integral, nodes that lie outside of a material boundary are automatically excluded from the sum since $m_i = 0$ for such nodes.

Once the nonlocal integral has been evaluated for a given plastic particle, a fixed-point expression, such as any of those discussed in Section 4.5, can be used to calculate an improved estimate for the local plastic multiplier, $\Delta\lambda_p^{k+1}$, where k is the iteration number. The nonlocal internal state variables are also updated using backward-Euler time integration of Eq. (4.24).

During the loop over the particles, the estimate from the previous iteration $\Delta\lambda_p^k$ can be removed from the grid nodes using

$$\Delta\lambda_i \leftarrow \Delta\lambda_i - \frac{m_p}{m_i}\phi_{ip}\Delta\lambda_p^k \tag{4.49}$$

for each grid node that receives information from the particle. The updated value of $\Delta\lambda_p$ can then be placed on these grid nodes using

$$\Delta\lambda_i \leftarrow \Delta\lambda_i + \frac{m_p}{m_i}\phi_{ip}\Delta\lambda_p^{k+1} \tag{4.50}$$

By immediately replacing $\Delta\lambda_p^k$ with $\Delta\lambda_p^{k+1}$ on the grid nodes, all remaining plastic particles for the iteration will be using the most up-to-date data, making the scheme a Gauss-Seidel iteration rather than a Jacobi iteration.

After each loop over the plastic particles, if the maximum value of $|\Delta\lambda_p^{k+1} - \Delta\lambda_p^k|$ is less than some specified tolerance, the solution is considered converged and the iteration scheme is terminated.

After a converged solution for the field of plastic multipliers has been computed, the nonlocal internal state variables must be updated for the *elastic* particles as well. This is due to the unique feature of nonlocal models that allows plastic deformation at a given particle to change the state of another particle a finite distance away, even if that particle is not undergoing plastic deformation itself. This phenomenon is called plastic diffusion. This also introduces the possibility that the yield surface of a particle that was initially considered to be elastic will contract due to plastic diffusion such that it begins to undergo plastic deformation. If this occurs, the particle must be reclassified as a plastic particle and the field of plastic multipliers must be recomputed, including the new plastic particle. As discussed in Section 4.4, this illustrates why nonlocal plasticity is best viewed as a complementarity problem where determining which particles are undergoing plastic deformation is an important nontrivial aspect of the solution.

4.7 Shear Band Localization Case Study

In this section, a simple 2D localization problem is solved to illustrate the effectiveness of the nonlocal MPM algorithm just described. As illustrated in Fig. 4.1, this problem consists of 4 meter wide and 5 meter tall rectangular plane strain plate with a symmetry (i.e., roller) boundary condition at the bottom and a one meter square region with reduced yield strength at the lower left-hand corner. The top surface of the plate is subject to a prescribed axial velocity, with all other velocity components on that surface set to zero. The lateral surfaces of the plate are traction free.

For all simulations, the bulk modulus is 76 GPa, the shear modulus is 26 GPa and

the yield strength, k_o, was set to 375 MPa in the weakened region, and 400 MPa in the rest of the domain. For both the local and overlocal cases, a von Mises model was used. This is equivalent to setting $\beta = \beta_p = 0$ in equation (4.34). This algorithm was implemented into the Uintah explicit dynamics MPM code [39]. This code along with the CPDI interpolation scheme [84] was used to solve the case study problem. Using this interpolation scheme, each particle domain is initially rectangular, and deforms into a parallelogram determined from the deformation gradient of the particle. The prescribed velocity of the top surface was chosen to be 7.5 m/s. Artificial viscosity was used to help dampen out the transient portion of the solution. The time step was chosen to be 20% of the Courant-Friedrichs-Lewy stable time step. For all mesh resolutions used, four material point particles were used in each cell, two in each direction.

4.7.1 Local Plasticity Solutions

The case study problem was first solved using a local von Mises plasticity model with linear softening. The local hardening modulus, h_η, was set to -4.0 GPa, where the negative sign indicates softening. Figure 4.2 shows a contour plot of the magnitude of the plastic strain tensor for a mesh spacing, h, of 0.5 m, 0.25 m, and 0.125 m. With all mesh resolutions, a shear band nucleates at the weakened region in the lower left-hand corner of the domain. The anomalous lack of convergence, as seen by the dependence of the shear band width on mesh size, and as further seen in the mesh-dependent post-peak stress-strain response of Fig. 4.3, is consistent with well-known observations from the literature using other analytical and numerical methods [28, 30].

4.7.2 Overlocal Plasticity Solutions

To illustrate the effectiveness of nonlocal theory at eliminating mesh sensitivity, the case study problem was solved using an overlocal von Mises plasticity model using the nonlocal MPM algorithm outlined in Section 4.6. The local hardening modulus was set to $h_\eta = 2$ GPa, and the nonlocal hardening modulus was set to $h_\zeta = -4$ GPa. This is equivalent to setting Stromberg and Ristinmaa's [51] overlocal parameter to

$m = 2$, with the hardening modulus set to $h = -2$ GPa. The nonlocal length scale was set to $L = 0.5$ m. With these values the nonlocal iteration scheme converged in fewer than seven iterations for each time step. Figure 4.4 shows contour plots of the magnitude of the plastic strain tensor using the overlocal model and three different mesh spacings. As the plots indicate, the shear band converges to a fixed width with mesh refinement. The width of the shear band is controlled by the nonlocal length scale. Unlike the results found using a local model, the overlocal stress-strain curve in Fig. 4.5 converges with mesh refinement. Specifically, the post-peak stress-strain response is driven by the problem geometry and material parameters rather than by the mesh spacing.

In addition to the convergence of the shear band width to a finite value, nonlocal models also have the advantage of being able to capture a size effect. Specifically, two structures of the same shape but different sizes will behave differently under the same applied tractions. With a nonlocal model, the ratio of the length scale associative with the problem geometry to the nonlocal length scale becomes a significant parameter. This is an important characteristic for a model to be capable of predicting large-scale problems based on small-scale laboratory experiments. To illustrate the size effect, the 2D plate case study was also solved using a specimen that is 8 meters wide and 10 meters high, which is exactly double the size of the original problem. The velocity at the top surface was prescribed to be 15 m/s, which is also exactly double the rate in the previous problem. The result is that the bulk strain rate in the plate is the same as with the original problem. The resulting apparent axial stress versus strain plot, along with that of the original problem, is shown in Fig. 4.6. Both the original problem and the scaled up problem were solved with a mesh resolution of $h = 0.25$ m. As the plot indicates, the apparent structural response for the problem with the larger length scale is more brittle than with the original problem. This illustrates the fact that a brittle structural response can result from either a large softening modulus, or from a material microstructure with a length scale much smaller than the structure's length scale.

4.8 Conclusion

Whereas nonlocal iteration schemes in the literature are typically specialized to apply to a particular choice of yield function, a general framework for deriving a nonlocal iterative solver has been elucidated in this work to apply to any general yield function. Moreover, a straightforward rigorous basis for deriving a corresponding convergence criterion scheme has been here developed using the Banach fixed-point theorem.

While these methods can be applied to any host code framework, they are particularly well suited to incorporation into the material point method (MPM). Specifically, by using the MPM background grid to evaluate the nonlocal integrals, there is no need to maintain a list of particles within the nonlocal neighborhood of a given particle. This attribute not only produces a matrix-free algorithm, but it is especially appealing for large-deformation problems in which the number and identity of material points in the vicinity of any given material point change in time.
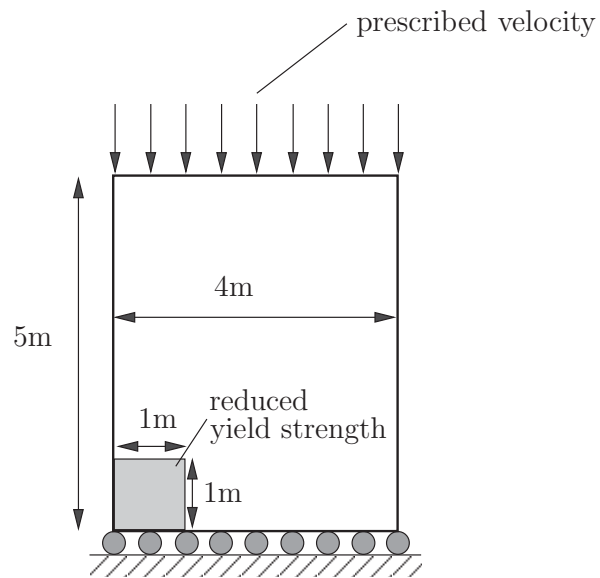
Figure 4.1. Schematic of the case study geometry. A symmetric boundary condition is used along the bottom surface, a prescribed velocity boundary condition is used along the top surface, and the lateral faces are stress free. The plate is in a state of plane strain.
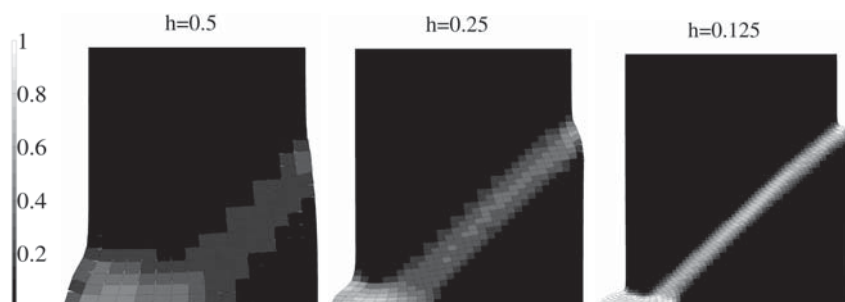
Figure 4.2. Contour plot of the magnitude of the plastic strain tensor using a local von Mises plasticity model with isotropic softening. The width of the shear band anomalously reduces with mesh spacing, h.
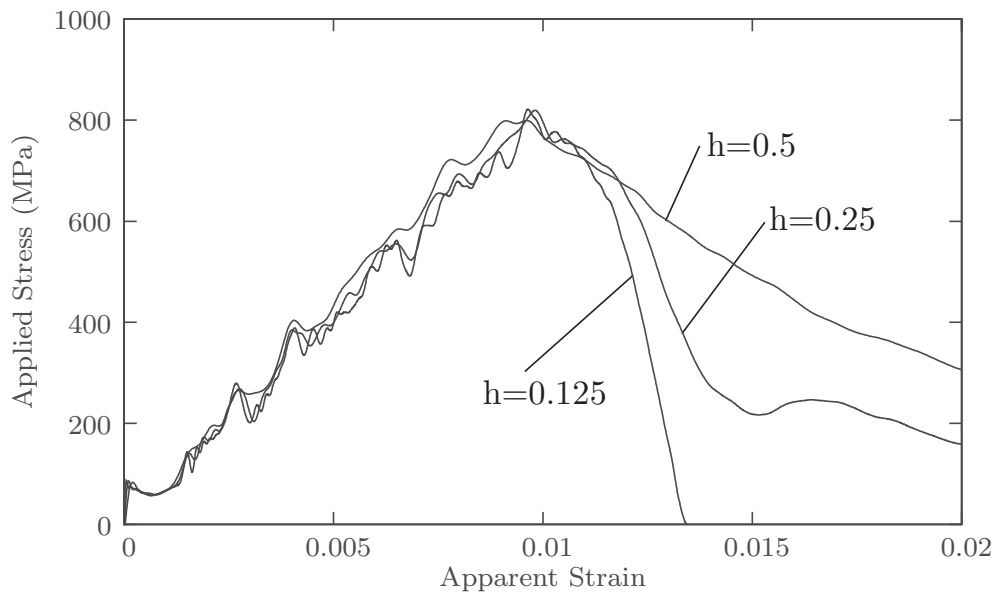
Figure 4.3. Nonconvergence of applied stress versus apparent axial strain (i.e., % change in plate height) when using a local von Mises plasticity model at three different mesh sizes, h.
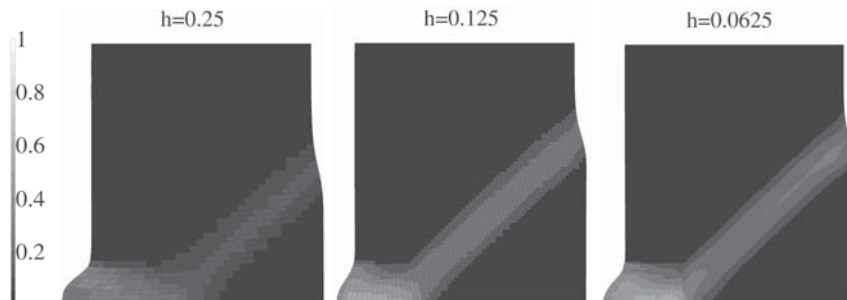
Figure 4.4. Contour plot of the magnitude of the plastic strain tensor using an overlocal von Mises plasticity model with isotropic softening, and a nonlocal length scale of 0.5m. Unlike the local model, the overlocal solution converges with mesh refinement.
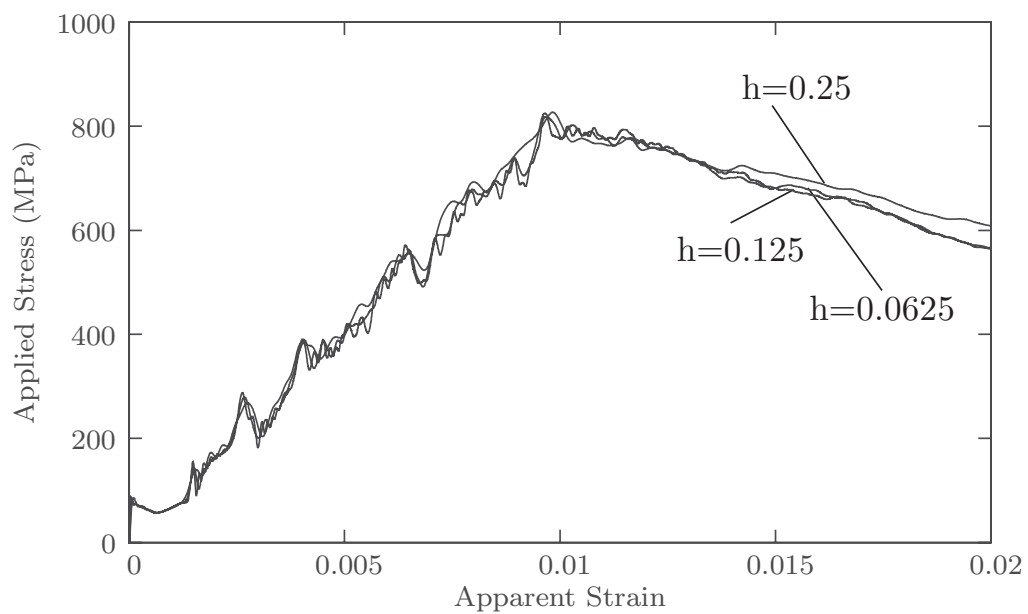
Figure 4.5. Plot of the applied stress versus apparent axial strain in the plate using an overlocal von Mises plasticity model with a nonlocal length scale of 0.5m and three different mesh resolutions, h, as indicated. With the overlocal model the stress/strain curve converges with mesh refinement.
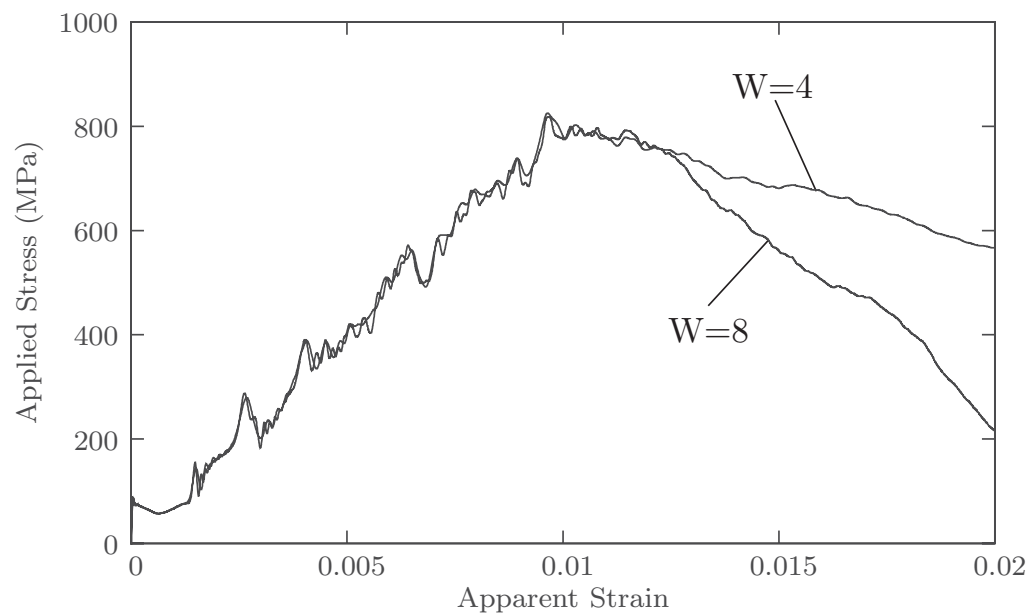
Figure 4.6. Plot of the applied stress versus apparent axial strain in the plate using an overlocal von Mises plasticity model with a nonlocal length scale of 0.5m and two different plate widths, W, as indicates. All other lengths have been scaled as well so that the two curves are for geometrically similar plates. The difference in the response is due to the size effect that results from nonlocal models.

Algorithm 1 Nonlocal plasticity algorithm for the material point method with a Drucker-Prager yield function

---

Step 1: Initialization

Initialize $\Delta\lambda_i \leftarrow 0$ at each grid node i.

for each particle p **do**

    Compute trial stress, and evaluate f_{trial} using Eq. (4.37)

    if $f_{\text{trial}} \geq 0$ **then**

        Compute initial guess for $\Delta\lambda_p$ by omitting $\langle\Delta\lambda\rangle_p$ in Eq. (4.41).

        Project $\Delta\lambda_p$ to the ith grid node using $\Delta\lambda_i \leftarrow \Delta\lambda_i + (m_p/m_i)\phi_{ip}\Delta\lambda_p$

    else

        $\Delta\lambda_p \leftarrow 0$

    end if

end for

Step 2: Main Iteration Loop

Initialize iteration counter: $k \leftarrow 0$

while ERROR > TOLERANCE **do**

    $k \leftarrow k + 1$

    for each plastic particle p **do**

        initialize: $\langle\Delta\lambda\rangle_p \leftarrow 0$, $M_p \leftarrow 0$

        for each node i within nonlocal support domain **do**

            $\langle\Delta\lambda\rangle_p \leftarrow \langle\Delta\lambda\rangle_p + \alpha(\boldsymbol{x}_p - \boldsymbol{x}_i)\Delta\lambda_i m_i$

            $M_\alpha \leftarrow M_\alpha + \alpha(\boldsymbol{x}_p - \boldsymbol{x}_i)m_i$

        end for

        $\langle\Delta\lambda\rangle_p \leftarrow \langle\Delta\lambda\rangle_p/M_\alpha;$ $\zeta^{n+1} \leftarrow \zeta^n + h_\zeta\langle\Delta\lambda\rangle_p$

        Calculate $\Delta\lambda_p^k$ using Eq. (4.39) or (4.41)

        Update stress using Eq. (4.49) and (4.50).

        $\eta^{n+1} \leftarrow \eta^n + h_\eta\Delta\lambda_p^k$

    end for

    ERROR $\leftarrow \max(|\Delta\lambda_p^k - \Delta\lambda_p^{k-1}|)$

end while

Step 3: Evaluate Nonlocal ISVs for elastic particles

for each elastic particle p **do**

    for each node i within nonlocal support domain **do**

        $\langle\Delta\lambda\rangle_p \leftarrow \langle\Delta\lambda\rangle_p + \alpha(\boldsymbol{x}_p - \boldsymbol{x}_i)\Delta\lambda_i m_i$

        $M_\alpha \leftarrow M_\alpha + \alpha(\boldsymbol{x}_p - \boldsymbol{x}_i)m_i$

    end for

    $\langle\Delta\lambda\rangle_p \leftarrow \langle\Delta\lambda\rangle_p/M_\alpha;$ $\zeta^{n+1} \leftarrow \zeta^n + h_\zeta\langle\Delta\lambda\rangle_p$

    $f_{\text{trial}} \leftarrow f(\boldsymbol{\sigma}_{\text{trial}}, \eta^n, \zeta^{n+1})$

    if $f_{\text{trial}} \geq 0$ **then**

        Add particle to list of plastic particles

    end if

end for

If the list of plastic particles changed, return to Step 2; otherwise stop.

CHAPTER 5

CONCLUSIONS

5.1 Novel Contributions to the Current State of Knowledge

This dissertation has advanced the current state of knowledge of plasticity theory in several important areas. Each subsection below describes one of these areas.

5.1.1 Effect of Nontraditional Plasticity Theories on the Sandler-Rubin Instability

As described in Chapter 2, the Sandler-Rubin instability is a physically unrealistic instability that may occur with any nonassociative plasticity model. When this instability is manifest, the governing equations become ill-posed, which results in mesh-dependent numerical solutions. Previous researchers had recognized the existence of this instability and ill-posedness, but no clear means of eliminating it (while maintaining agreement with experimental data) had been provided. In Chapter 2, the effect of three nontraditional plasticity models on this instability were investigated. These nontraditional models included a viscoplastic model, an incrementally nonlinear model, and a nonlocal model. Numerical and analytical analyses demonstrated that, of these models, only the incrementally nonlinear model is capable of eliminating the instability while maintaining agreement with existing experimental data.

5.1.2 Validation of Incrementally Nonlinear Plasticity Theory

While incrementally nonlinear plasticity theory was shown to eliminate the Sandler-Rubin instability, traditional material characterization tests are incapable of distinguishing between incrementally linear and incrementally nonlinear material response. Therefore, new experimental techniques are required to validate incrementally non-

linear models. A new experimental method and a new data analysis technique for studying the incremental response of materials were presented in Chapter 3. These new techniques were used to study the incremental response of aluminum 6061-T0. This study suggested that there is significant nonlinearity in the incremental response of this material, though additional experimental investigation using nonmonotonic loading is warranted to gain greater accuracy and precision. Moreover, since direct measurement of tangent tensors requires measuring material response for multiple loading directions, and since measuring the response for one loading direction can irreversibly alter the material microstructure (to preclude knowing with certainty the response to a different loading direction), advances in mesoscale modeling may be critical to validate the new data analysis method.

5.1.3   A Nonlocal Plasticity Algorithm for the Material Point Method

One of the nontraditional plasticity theories studied in Chapter 2 is a nonlocal theory. The reason for investigating nonlocal effects on the Sandler-Rubin instability is that nonlocal theory has been known to resolve other problems (e.g., nonconvergence with localization problems) that occur with traditional plasticity theories, as well as the unique dispersive wave propagation behavior predicted by nonlocal models. While nonlocal theory is a well-established means of regularizing otherwise ill-posed localization problems, there have been few efficient numerical schemes developed for solving the equations of nonlocal plasticity. Schemes have previously been developed for solving these equations using finite-element or element-free Galerkin methods, but no general convergence criteria had been developed for these methods. A new numerical scheme for solving these equations using the material point method (MPM) was presented in Chapter 4. This is the first nonlocal plasticity algorithm that has been developed for the MPM. The new algorithm exploits unique features of the MPM to result in a simple and efficient algorithm. A new convergence criterion was derived that is not only applicable to the new method, but was also shown to be applicable to some of the finite-element methods developed previously. The new method was implemented in the Uintah MPM code, and a classical localization problem was

solved. It was demonstrated that the new algorithm produces mesh-independent solutions, whereas with a traditional local plasticity theory the solution is mesh dependent.

5.2 Suggestions for Future Work

The new developments reported in this dissertation suggest several avenues for further research. Incrementally nonlinear and nonlocal plasticity theories are both relatively new theories, and have yet to be incorporated into mainstream engineering analysis. A significant impediment to more widespread adoption of both incrementally nonlinear and nonlocal theory has been a lack of established testing methods to parameterize and further validate these models. For example, incrementally nonlinear plasticity results in at least one new material parameter that controls how much the loading direction influences the plastic flow direction. Nonlocal plasticity theory requires the specification of an intrinsic length scale associated with a material. While it is clear that this length scale is tied to the size of localization regions that can easily be measured in the laboratory, no theory has yet been developed that accounts for how the size of this localization region changes with respect to loading conditions, such as confining pressure or the loading rate.

The new techniques described in Chapter 3 may play an important role in both further validation and parameterization of incrementally nonlinear models such as the extended flow rule (EFR) used in Chapter 2. Because of the limited number of tests reported in Chapter 3, more tests of that type need to be performed to confirm the trends observed in that chapter. Furthermore, additional theoretical analysis is needed to validate or invalidate the assumptions made in the interpolation scheme presented in Chapter 3. As described in that chapter, the most general way of describing history-dependent nonlinear material response is using a functional of the deformation history. A starting point for validating the proposed interpolation scheme would be to identify some of the mathematical properties of such a constitutive response functional. For example, if it could be shown that the constitutive functional is a bounded linear functional. Then the Riesz Representation Theorem could be used to represent the functional as the inner product of the deformation history function

with some kernel function. There are many other theorems that apply to bounded linear functionals and could help to prove or disprove the appropriateness of the proposed interpolation scheme.

In addition to the reformulations of classical theory that were investigated in Chapter 2, there are other alternative theories that merit further investigation. For example, a new variational formulation by Krabbenøft [89] dispenses with the need to specify a separate plastic potential function, allows arbitrary stress-dilatancy relations, and results in a symmetric plastic tangent stiffness tensor. As discussed in Chapter 2, loss of symmetry of the tangent stiffness tensor is what allows both the shear banding and Sandler-Rubin instability to develop. Therefore, this new theory may provide a means of eliminating the instability while also matching existing data.

In addition to developing and validating new theories, as suggested in Chapter 4, improved numerical schemes are needed to solve the equations that result from these new theories. Specifically, the new iterative scheme presented in Chapter 4 will diverge for extremely large values of the softening modulus. The development of an alternative iterative scheme that increases the convergence range of this scheme would be helpful. As was suggested in that chapter, a combination of a global fixed-point iteration with a local Newton iteration scheme has been used in other applications [87], and may prove advantageous for nonlocal plasticity. Also, an over/under relaxation scheme ought to be investigated as a means of accelerating convergence. Finally, the nonlocal MPM formulation presented in this dissertation has only been applied to the MPM with an explicit time integrator. For many applications, it would be useful to extend the applicability of this iteration scheme to the MPM with an implicit time integrator.

REFERENCES

[1] Hadamard, J., 1902. "Sur les problèmes aux dérivés partielles et leur signification physique," Princeton University Bulletin, **13**, pp. 49–52.

[2] Brannon, R. M., 2007. "Elements of phenomenological plasticity: Geometrical insight, computational algorithms, and topics in shock physics," In *ShockWave Science and Technology Reference Library*, Y. Horie, ed. Springer Berlin Heidelberg, pp. 225–274.

[3] Drucker, D., and Prager, W., 1952. "Soil mechanics and plastic analysis or limit design," Quarterly of Applied Mathematics, **10**(2), pp. 157 – 165.

[4] Lade, P. V., Nelson, R. B., and Ito, Y. M., 1987. "Nonassociated flow and stability of granular materials," Journal of Engineering Mechanics, **113**(9), pp. 1302–1318.

[5] Poorooshasb, H., 1966. "Yielding and flow of sand in triaxial compression: Part 1," Canadian Geotechnical Journal, **3**(4), p. 179.

[6] Spitzig, W. A., Sober, R. J., and Richmond, O., 1975. "Pressure dependence of yielding and associated volume expansion in tempered martensite," Acta Metallurgica, **23**(7), pp. 885–93.

[7] Spitzig, W. A., Sober, R. J., and Richmond, O., 1976. "The effect of hydrostatic pressure on the deformation behavior of maraging and hy-80 steels and its implications for plasticity theory," Metallurgical Transactions A (Physical Metallurgy and Materials Science), **7A**(11), pp. 1703–10.

[8] Spitzig, W. A., 1979. "Effect of hydrostatic pressure on plastic-flow properties of iron single crystals," Acta Metallurgica, **27**(4), pp. 523–34.

[9] Richmond, O., and Spitzig, W. A., 1980. "Pressure dependence and dilatancy of plastic flow," In Proceeding of the Fifteenth International Congress on Theoretical and Applied Mechanics, pp. 377–86.

[10] Dunand, M., and Mohr, D., 2011. "On the predictive capabilities of the shear modified gurson and the modified Mohr-Coulomb fracture models over a wide range of stress triaxialities and lode angles," Journal of the Mechanics and Physics of Solids, **In Press**.

[11] Mohr, D., Dunand, M., and Kim, K.-H., 2010. "Evaluation of associated and non-associated quadratic plasticity models for advanced high strength steel sheets under multi-axial loading," International Journal of Plasticity, **26**(7), pp. 939 – 956.

[12] Hill, R., 1958. "A general theory of uniqueness and stability in elastic-plastic solids," Journal of the Mechanics and Physics of Solids, **6**(3), p. 236.

[13] Drucker, D., 1950. "Some implications of work hardening and ideal plasticity," Quarterly of Applied Mathematics, **7**(4), pp. 411–418.

[14] Schreyer, H., and Neilsen, M., 1996. "Analytical and numerical tests for loss of material stability," International Journal for Numerical Methods in Engineering, **39**(10), pp. 1721 – 1736.

[15] Brannon, R., and Drugan, W., 1993. "Influence of non-classical elastic-plastic constitutive features on shock wave existence and spectral solutions," Journal of the Mechanics and Physics of Solids, **41**(2), pp. 297 – 297.

[16] Pučik, T., Brannon, R., and Burghardt, J. "Nonuniqueness and instability of classical formulations of nonassociative plasticity, part 1: case study," under review in the International Journal of Plasticity.

[17] Il'Yushin, A., 1961. "On postulate of plasticity," PMM: Journal of Applied Mathematics and Mechanics, **25**(3), pp. 746 – 752.

[18] Neilsen, M., and Schreyer, H., 1993. "Bifurcations in elastic-plastic materials," International Journal of Solids and Structures, **30**(4), pp. 521 – 44.

[19] Rudnicki, J., and Rice, J. R., 1975. "Conditions for the localization of deformation in pressure-sensitive dilatant materials," Journal of the Mechanics and Physics of Solids, **23**(6), p. 371.

[20] Runesson, K., and Mroz, Z., 1989. "A note on nonassociated plastic flow rules," International Journal of Plasticity, **5**(6), pp. 639–58.

[21] Bigoni, D., and Hueckel, T., 1991. "Uniqueness and localization-1. associative and non-associative elastoplasticity," International Journal of Solids and Structures, **28**, pp. 197–213.

[22] Rice, J. R., 1976. "The localization of plastic deformation," In Proceedings of the 14th International Congress on Theoretical and Applied Mechanics, W. Koiter, ed., North-Holland Publishing Company, pp. 207–220.

[23] Bigoni, D., 1995. "On flutter instability in elastoplastic constitutive models," International Journal of Solids and Structures, **32**(21), pp. 3167 – 89.

[24] Vermeer, P., 1982. "Simple shear-band analysis using compliances," In Deformation and failure of granular materials, P. A. Vermeer and H. J. Luger, eds., International Union of Theoretical and Applied Mechanics, A.A. Balkema, Rotterdam, Netherlands, pp. 493 – 499.

[25] Molenkamp, F., 1985. "Comparison of frictional material models with respect to shear band initiation," Geotechnique, **35**(2), pp. 127 – 143.

[26] Valanis, K., 1989. "Banding and stability in plastic materials," Acta Mechanica, **79**(1-2), pp. 113 – 141.

[27] Valanis, K. C., 1996. "Ill-posedness of the initial and boundary value problems in non-associative plasticity," Acta Mechanica, **114**, pp. 1–25.

[28] Bažant, Z. P., 1976. "Instability, ductility, and size effect in strain-softening concrete," ASCE J. Eng. Mech. Div., **102**(2), pp. 331 – 344.

[29] Belytschko, T., and Bazant, Z., 1984. "Strain-softening materials and finite element solutions," In Constitutive Equations: Macro and Computational Aspects; presented at the Winter Annual Meeting of the American Society of Mechanical Engineers, pp. 253 – 272.

[30] de Borst, R., Sluys, L., Muhlhaus, H., and Pamin, J., 1993. "Fundamental issues in finite element analyses of localization of deformation," Engineering Computations, **10**, pp. 99–121.

[31] Sandler, I., and Rubin, D., 1987. "The consequences of non-associated plasticity in dynamic problems," In *Constitutive Laws for Engineering Materials*. Elsevier Science Publishing Co. Inc., Amsterdam, pp. 345–353.

[32] Sandler, I., and Pučik, T., 1993. "Non-uniqueness in dynamic rate-independent non-associated plasticity," Tech. Rep. DNA-TR-92-108, Defense Nuclear Agency, Alexandria, VA 22310-3398.

[33] Stoughton, T. B., 2002. "A non-associated flow rule for sheet metal forming," International Journal of Plasticity, **18**(5-6), pp. 687 – 714.

[34] Taherizadeh, A., Green, D. E., Ghaei, A., and Yoon, J.-W., 2010. "A non-associated constitutive model with mixed iso-kinematic hardening for finite element simulation of sheet metal forming," International Journal of Plasticity, **26**(2), pp. 288 – 309.

[35] Dorgan, R. J., 2006. "A mixed finite element implementation of a gradient-enhanced coupled damage–plasticity model," International Journal of Damage Mechanics, **15**(3), p. 201.

[36] Valanis, K. C., 1998. "Diffusion potential and well-posedness in non-associative plasticity," International Journal of Solids and Structures, **35**, pp. 5173–5188.

[37] Stoughton, T., 2006. "Review of Drucker's postulate and the issue of plastic stability in metal forming," International Journal of Plasticity, **22**(3), p. 391.

[38] Stoughton, T., 2008. "On the existence of indeterminate solutions to the equations of motion under non-associated flow," International Journal of Plasticity, **24**(4), p. 583.

[39] de St. Germain, J., McCorquodale, J., Parker, S., and Johnson, C., 2000. "Uintah: A massively parallel problem solving environment," In Ninth IEEE International Symposium on High Performance and Distributed Computing, IEEE, Piscataway, NJ, pp. 33–41.

[40] Sulsky, D., 1994. "A particle method for history-dependent materials," Computer Methods in Applied Mechanics and Engineering, **118**(1-2), p. 179.

[41] Bardenhagen, S., and Kober, E., 2004. "The generalized interpolation material point method," Comput. Model. Eng. Sci., **5**(6), pp. 477–495.

[42] Anandarajah, A., 1995. "Incremental stress-strain behavior of granular soil," Journal of Geotechnical Engineering, **121**(1), p. 57.

[43] Tamagnini, C., Calvetti, F., and Viggiani, G., 2005. "An assessment of plasticity theories for modeling the incrementally nonlinear behavior of granular soils," Journal of Engineering Mathematics, **52**(1-3), pp. 265–91.

[44] Nicot, F., and Darve, F., 2007. "Basic features of plastic strains: From micro-mechanics to incrementally nonlinear models," International Journal of Plasticity, **23**(9), pp. 1555–88.

[45] Hashiguchi, K., 1997. "The extended flow rule in plasticity," International Journal of Plasticity, **13**(1-2), p. 37.

[46] Bauer, E., 1996. "Calibration of a comprehensive hypoplastic model for granular materials," Soils and Foundations, **36**(1), pp. 13–26.

[47] Gudehus, G., 1996. "Comprehensive constitutive equation for granular materials," Soils and Foundations, **36**(1), pp. 1–12.

[48] Ito, K., 1979. "New flow rule for an elastic-plastic solid based on kbw model with a view to lowering the buckling stresses of plates or shells," Technology Reports of the Tohoku University, **44**(2), pp. 199–232.

[49] Sluys, L., de Borst, R., and Huhlhaus, H., 1993. "Wave propagation, localization and dispersion in a gradient-dependent medium," International Journal of Solids and Structures, **30**(9), pp. 1153–1171.

[50] Di Luzio, G., and Bažant, Z., 2005. "Spectral analysis of localization in nonlocal and over-nonlocal materials with softening plasticity or damage," International Journal of Solids and Structures, **42**(23), pp. 6071 – 100.

[51] Stromberg, L., and Ristinmaa, M., 1996. "Fe-formulation of a nonlocal plasticity theory," Computer Methods in Applied Mechanics and Engineering, **136**, pp. 124–144.

[52] Brannon, R., Burghardt, J., Bronowski, D., and Bauer, S., 2009. "Experimental assessment of unvalidated assumptions in classical plasticity theory," Tech. Rep. SAND2009-0351, Sandia National Laboratory, Albuquerque, New Mexico 87185.

[53] Gordon, M., and Xabier Garaizar, F., 1999/06/. "Wave speeds for an elasto-plastic model for two-dimensional deformations with a nonassociative flow rule," Quarterly of Applied Mathematics, **57**(2), pp. 245 – 50.

[54] Nova, R., 1994. "Controlability of the incremental response of soil specimens subjected to arbitrary loading programs," Journal of Mechanical Behavior of Materials, **5**(2), pp. 193–201.

[55] Chambon, R., 2005. "Some theoretical results about second-order work, uniqueness, existence and controllability independent of the constitutive equation," Journal of Engineering Mathematics, **52**(1), p. 53.

[56] Royis, P., and Doanh, T., 1998. "Theoretical analysis of strain response envelopes using incrementally non-linear constitutive equations," International Journal for Numerical Methods in Geomechanics, **22**, pp. 97–132.

[57] Alonso-Marroquin, F., 2002. "Calculation of the incremental stress-strain relation of a polygonal packing," Physical Review E, **66**(2), p. 021301.

[58] Hashash, Y. M. A., Yao, J. I.-C., and Wotring, D. C., 2003. "Glyph and hyperstream representation of stress and strain tensors and material constitutive response," Int. J. Numer. Anal. Meth. Geomech., **27**, pp. 603–626.

[59] Gudehus, G., 1979. "A comparison of some constitutive laws for soils under radially symmetric loading and unloading," In 3rd International Conference on Numerical Methods in Geomechanics, Aachen and Wittke, eds., Vol. 4, Balkema Publisher, pp. 1309–1324.

[60] Brannon, R., Fossum, A., and Strack, O., 2009. *KAYENTA: Theory and User's Guide*, sand2009-2282 ed. Sandia National Laboratories, March.

[61] Steffen, M., Wallstedt, P., Guilkey, J., Kirby, R., and Berzins, M., 2008. "Examination and analysis of implementation choices within the material point method (MPM)," CMES - Computer Modeling in Engineering and Sciences, **31**(2), pp. 107–127.

[62] Guilkey, J., and Weiss, J., 2003. "Implicit time integration for the material point method: quantitative and algorithmic comparisons with the finite element method," International Journal for Numerical Methods in Engineering, **57**(9), pp. 1323 – 38.

[63] Sulsky, D., and Kaul, A., 2004. "Implicit dynamics in the material-point method," Computer Methods in Applied Mechanics and Engineering, **193**(12-14), pp. 1137 – 70.

[64] York, A., Sulsky, D., and Schreyer, H., 1999. "The material point method for simulation of thin membranes," International Journal for Numerical Methods in Engineering, **44**, pp. 1429–1456.

[65] Love, E., and Sulsky, D., 2005. "An energy-consistent material-point method for dynamic finite deformation plasticity," International Journal for Numerical Methods in Engineering, **65**, pp. 1608–1638.

[66] Nairn, J., 2003. "Material point method calculations with explicit cracks," Computer Modeling in Engineering and Sciences, **4**, pp. 649–663.

[67] Guo, Y., and Nairn, J., 2006. "Three-dimensional dynamic fracture analysis using the material point method," Computer Modeling in Engineering and Sciences, **16**, pp. 141–155.

[68] Ma, S., Zhang, X., and Qiu, X., 2009. "Comparison study of mpm and sph in modeling hypervelocity impact problems," International Journal of Impact Engineering, **36**, pp. 272–282.

[69] Burghardt, J., Leavy, B., Guilkey, J., Xue, Z., and Brannon, R., 2010. "Application of uintah-mpm to shaped charge jet penetration of aluminum," IOP Conference Series: Materials Science and Engineering, **10**, p. 012223 (9 pp.).

[70] Bažant, Z. P., and Zubelewicz, A., 1988. "Strain-softening bar and beam: exact non-local solution," Int. J. Solids Structures, **7**(7), pp. 659–673.

[71] Erigen, A. C., 1981. "On nonlocal plasticity," International Journal of Engineering Science, **19**, pp. 1461–1474.

[72] Bažant, Z. P., and Lin, F.-B., 1988. "Non-local yield limit degredation," International Journal for Numerical Methods in Engineering, **26**, pp. 1805–1823.

[73] Belytschko, T., and Kulkarni, M., 1990. "On imperfections and spatial gradient regularization in strain softening viscoplasticity," In Failure criteria and analysis in dynamic response; presented at the Winter Annual Meeting of the American Society of Mechanical Engineers, Vol. 107, pp. 1–5.

[74] Aifantis, E., 1999. "Strain gradient interpretation of size effects," International Journal of Fracture, **95**, pp. 299–314.

[75] Bažant, Z. P., and Pang, S.-D., 2007. "Activation energy based extreme value statistics and size effect in brittle and quasibrittle fracture," Journal of the Mechanics and Physics of Solids, **55**(1), pp. 91 – 131.

[76] Engelen, R. A., Geers, M. G., and Baaijens, F. P., 2003. "Nonlocal implicit gradient-enhanced elastoplasticity for the modeling of softening behavior," International Journal of Plasticity, **19**, pp. 403–433.

[77] Geers, M., 2004. "Finite strain logarithmic hyperelasto-plasticity with softening: a strongly non-local implicit gradient framework," Computer Methods in Applied Mechanics and Engineering, **193**(30-32), p. 3377.

[78] De Borst, R., and Muehlhaus, H.-B., 1992. "Gradient-dependent plasticity: Formulation and algorithmic aspects," International Journal for Numerical Methods in Engineering, **35**(3), pp. 521 – 539.

[79] Peerlings, R., Geers, M., de Borst, R., and Brekelmans, W., 2001. "A critical comparison of nonlocal and gradient-enhanced softening continua," International Journal of Solids and Structures, **38**, pp. 7723–7746.

[80] Bažant, Z. P., and Jirasek, M., 2002. "Nonlocal integral formulations of plasticity and damage: Survey of progress," Journal of Engineering Mechanics, **128**, pp. 1119–1149.

[81] Chen, J.-S., Wu, C.-T., and Belytschko, T., 2000. "Regularization of material instabilities by meshfree approximations with intrinsic length scales," International Journal for Numerical Methods in Engineering, **47**(7), pp. 1303–22.

[82] Pan, X., and Yuan, H., 2009. "Nonlocal damage modelling using the element-free galerkin method in the frame of finite strains," Computational Materials Science, **46**(3), pp. 660 – 666.

[83] Weckner, O., Silling, S., and Askari, A., 2009. "Dispersive wave propagation in the nonlocal peridynamic theory," In ASME International Mechanical Engineering Congress and Exposition, Proceedings, Vol. 12, pp. 503 – 504.

[84] Sadeghirad, A., Brannon, R. M., and Burghardt, J., 2011. "A convected particle domain interpolation technique to extend applicability of the material point method for problems involving massive deformations," International Journal for Numerical Methods in Engineering, **86**(12), pp. 1435–1456.

[85] Jirasek, M., and Rolshoven, S., 2003. "Comparison of integral-type nonlocal plasticity models for strain-softening materials," International Journal of Engineering Science, **41**(13-14), pp. 1553 – 602.

[86] Wallstedt, P., and Guilkey, J., 2008. "An evaluation of explicit time integration schemes for use with the generalized interpolation material point method," Journal of Computational Physics, **227**(22), pp. 9628 – 42.

[87] Ortega, J. M., and Rheinboldt, W. C., 2000. *Iterative solution of nonlinear equations in several variables* Society for Industrial and Applied Mathematics, Philadelphia, PA, USA.

[88] Simó, J., and Hughes, T., 1998. *Computational inelasticity* Interdisciplinary Applied Mathematics: Mechanics and Materials. Springer.

[89] Krabbenhøft, K., 2009. "A variational principle of elastoplasticity and its application to the modeling of frictional materials," International Journal of Solids and Structures, **46**(3-4), pp. 464 – 79.